Sensitivities of atmospheric composition and climate to altitude and latitude of hypersonic aircraft emissions

Johannes Pletzer[1,2], Volker Grewe[1,2]

[1]Deutsches Zentrum für Luft- und Raumfahrt, Institut für Physik der Atmosphäre, Oberpfaffenhofen, Germany
[2]Delft University of Technology, Aircraft Noise and Climate Effects, Delft, The Netherlands

Correspondence to: Johannes Pletzer (johannes.pletzer@posteo.com)

Abstract. Hydrogen-powered hypersonic aircraft are designed to travel in the middle stratosphere at approximately 30-40 km. These aircraft can have a considerable impact on climate-relevant species like stratospheric water vapour, ozone and methane and thus would contribute to climate warming. The impact of hypersonic aircraft emissions on atmospheric composition and in turn on radiation fluxes differs strongly depending on cruise altitude. However, in contrast to variation of altitude of emission, differences from variation of latitude of emission are currently unknown. Using an atmospheric chemistry general circulation model, we show that a variation in latitude of emission can have a larger effect on perturbations and stratospheric-adjusted radiative forcing than a variation of altitude of emission. Our results include individual impacts on middle atmospheric water vapour, ozone and methane, of water vapour and nitrogen oxide emissions, as well as unburnt hydrogen, and the resulting radiative forcing. Water vapour perturbation lifetime continues the known tropospheric increase with altitude and reaches almost six years in the middle stratosphere. Our results demonstrate how atmospheric composition changes caused by emissions of hypersonic aircraft are controlled by large-scale processes like the Brewer-Dobson circulation and, depending on latitude of emission, local phenomena like polar stratospheric clouds.

The analysis includes a model evaluation of ozone and water vapour with satellite data and a novel approach to reduce simulated years by one-third. A prospect for future hypersonic research is the analysis of seasonal sensitivities and simulations with emissions from combustion of liquefied natural gas instead of liquid hydrogen.

1. Introduction

Since the civil supersonic aircraft Concorde and Tupolev Tu-144 entered and left service (1969-2003), some time has passed. In the meantime, new projects appeared that intend to solve the predecessors' problems, which were mainly the large cost, the significant contribution to climate warming and the loud noise. More than a few manufactures, e.g. *Boom Technology*[1] or *Spike*

---

[1] https://boomsupersonic.com/company

Aerospace[2]*,* are on their way to deliver supersonic aircraft for commercial use. But, to our knowledge, a full-scale prototype has not been announced until today by any of the manufacturers.

Technically there are three categories of aircraft: subsonic aircraft that fly slower than the speed of sound, supersonic aircraft, whose speed exceeds the speed of sound, whereas the speed of hypersonic aircraft is at least five times the speed of sound. The supersonic aircraft design with the best market potential is a small scale business jet for customers that value time greatly (Sun and Smith, 2017; Liebhardt et al., 2011). Hence, the biggest benefit of and best sale argument for supersonic business jets are their speed and their travel time. For the same distance, the travel time of supersonic aircraft is advertised as approximately half that of subsonic aircraft. Of course, the different supersonic aircraft designs each have their specific speed and may deviate from this number. In comparison, hypersonic aircraft, which are in development, but not as technologically advanced as supersonic aircraft, fly at higher altitudes and higher speed compared to supersonic aircraft. Hence, they reduce travel time by a factor four to eight instead of two.

Clearly, on one hand, the aircraft industry strives to satisfy customer's needs with potential innovations like super- and hypersonic aircraft. On the other hand, however, aircraft industry currently is in a transformation process to build a climate compatible aircraft infrastructure. It easily takes decades to develop new aircraft before they can be launched on the market and the lifetime of aircraft can also be counted in decades. Hence, the climate compatibility of new aircraft has a long-lasting effect and is therefore of utmost importance.

Generally, numerous estimates of the climate impact and the growth potential of the current aircraft industry have been published (Lee et al., 2021; Fahey et al., 2016; Pachauri, R.K. and Reisinger, A. (Eds.), 2007; Pachauri, R.K and Meyer, L.A. (Eds.), 2014). One of the newest estimates analyses both, the climate impact and the growth potential, using projections of different technological development scenarios (Grewe et al., 2021).

The impact on atmosphere and climate of potential fleets of supersonic aircraft that could replace parts of a conventional fleet, has been estimated and reviewed in many - some very extensive - publications (Grewe et al., 2010; Zhang et al., 2021a; Penner, J.E. et al., 1999; Matthes et al., 2022). In contrast, first publications about atmospheric perturbation and climate impact of hypersonic aircraft have only appeared more recently (Ingenito, 2018; Kinnison et al., 2020; Pletzer et al., 2022).

Briefly summarized for supersonic and hypersonic aircraft, the non-CO_2 effect, mainly water vapour (H_2O), contributes more to climate impact with increasing altitude due to the longer H_2O perturbation lifetime and the resulting radiative forcing and climate impact per revenue passenger kilometer is manifold that of subsonic aircraft (Grewe et al., 2010; Pletzer et al., 2022).

---

[2] https://www.spikeaerospace.com/

The depletion of the ozone (O_3) layer is significant, however, the altitude dependency of the radiative forcing to emission altitude is more complex for O_3 than for H_2O (Zhang et al., 2021a, b).

Since the development of high-flying aircraft is clearly continuing, the application of mitigation options for the lowest possible climate impact during commercial use are crucial and should be fully exploited. That is not only in case these aircraft really are in use one day, but also to estimate the optimization potential beforehand. The technological reality that any fuel will ultimately increase the concentration of the main climate driver H_2O seems inevitable, since purely battery-powered aircraft are not a viable option for distances that super- and hypersonic aircraft can cover in a single flight due to the batteries weight. Taking 100 % sustainable alternative fuels provides the option of net-zero CO_2 emission flights, although availability and the degree of sustainability is likely to be a limitation for the coming decades, and non-CO_2 effects remain. Therefore, the importance of improving in-flight climate efficiency of fueled aircraft cannot be emphasized enough. The potential of climate optimized routing for conventional aircraft (Grewe et al., 2014a; Grewe et al., 2014b; Sridhar et al., 2011; Matthes et al., 2012, 2020) and climate optimized design (Grewe et al., 2017; Dahlmann et al., 2016) has been shown before. To achieve the same for high-flying aircraft, it is key to analyze sensitivities at stratospheric altitudes i.e. the impact of aircraft emissions on atmospheric composition and climate depending on latitude and altitude of emission.

Therefore, in this study, we performed 24 simulations and a reference simulation with the Atmospheric-Chemistry General Circulation Model ECHAM/MESSy (EMAC), addressing a wide range of sensitivities. The simulations include emission scenarios where H_2O, NO_x and H_2 are emitted separately at two altitudes (30 km, 38 km) and four latitude regions (southern mid-latitudes, tropics, northern mid-latitudes, north polar). The atmospheric composition changes are then used to calculate the radiative forcing with EMAC.

The paper is structured as follows. In section two, we present the EMAC model and the simulation setup including a model evaluation with H_2O and O_3 satellite measurements and a novel approach to reduce simulation cost. Section three addresses the variation of emission in latitude and altitude and the emissions' magnitude. The direct and indirect effects of emissions, H_2O, NO_x and H_2, on atmospheric composition is shown in section four. Section five focuses on the radiative forcing from the atmospheric composition changes, followed by a discussion of atmospheric and radiative sensitivities in section six, a general discussion in section seven and a summary.

2. Methods and simulations

2.1. EMAC

We used ECHAM5/MESSy to calculate atmospheric composition changes and radiative forcing. ECHAM5 is the dynamical core of EMAC and used to calculate the atmospheric general circulation (Roeckner et al., 2006). MESSy, version 2.54.0 of the

Modular Earth Model System (Jöckel et al., 2005; 2006; 2010; 2016), extends ECHAM5 with its modular infrastructure and 'plug-in' submodels. Overall, ECHAM5/MESSy is able to combine the atmosphere, ocean and land domain and the chemistry within MESSy is interconnected with these three domains. The applied Atmospheric Chemistry General Circulation Model (AC-GCM) setup, is presented in the following subsection and follows the setup already presented in Pletzer et al. (2022). The model setup is from here on referred to as "HS-sens".

2.2. EMAC model setup

The applied horizontal resolution is T42 (triangular truncation at wave number 42) for the dynamical core, which relates to a Gaussian grid of approximately 2.8° x 2.8° in longitude and latitude. The vertical resolution includes 90 levels from the surface to 0.01 hPa (center of the uppermost layer) of the middle atmosphere (MA) at approximately 80 km. The complete resolution description is abbreviated as T42L90MA. The setup combines boundary conditions of 2050 surface emissions and nudging to present day meteorology.

Table 1: Overview of key properties used in the model setup.

Model properties	Model setup HS-sens
General Circulation Model	ECHAM5
Grid cells (latitude x longitude x level)	64 x 128 x 90
Vertical model domain	Surface to 0.01 hPa (approx. 80 km)
Meteorology	Present day, specified dynamics
Vertical nudging domain	Surface(4th model layer) to 10 hPa
Nudging data	ERA-Interim (2007-2016)
Nudged variables	Divergence, vorticity, log(surface pressure)
Lower boundary conditions	CCMI RCP6.0

2.2.1 Specified dynamics

We used specified dynamics i.e. we nudged towards ERA-Interim reanalysis data. This Newtonian relaxation is applied for the GCM variables divergence with a relaxation timescale of 48 h, vorticity (6 h) and the logarithm of the surface pressure (24 h). The domain, where nudging is applied, ranges from the 4th model layer above the ground to approximately 10 hPa. Note that the impact of a 2050 meteorology would be – coarsely estimated – a 8-10 % strengthening of the middle atmospheric circulation, which would reduce atmospheric perturbations from hypersonic aircraft accordingly (subsubsection 7.1.2, Pletzer et al., 2022).

2.2.1 Lower boundary conditions

The potential entry-into-service of hypersonic aircraft is approximately 2050. Hence, the CCMI RCP6.0 scenario was applied to simulate atmospheric conditions starting 2050. The relevant surface emissions were included as lower boundary conditions and added to the internal tracers. Only aircraft emission scenarios were excluded.

2.2.3 Model evaluation

Temperature, O_3 and H_2O representation of the upper troposphere-lower stratosphere (UTLS) region in EMAC were evaluated before using aircraft measurements (Pletzer et al., 2022). We kindly ask the reader to refer to this publication for detailed information. To summarize briefly, the key message for EMAC is, firstly, a systematic cold bias of -3.8 to -2.5 K in the extra-tropics, responsible for an upward shift of the tropopause and as a consequence an under- and overestimation of O_3 and H_2O mixing ratios, respectively. Secondly, the Taylor correlation coefficient, estimating correlation between observations and model results in the UTLS, is $r \sim 0.90$ for H_2O and $r \sim 0.95$ for O_3 and temperature. In this publication, we extend the verification region to higher altitudes with satellite measurements published as the 'Stratospheric Water and OzOne Satellite Homogenized data set' SWOOSH by Davis et al. (2016). Further information is presented in the following subsection 2.3.

2.3. Evaluation with satellite data (SWOOSH)

The satellite dataset SWOOSH contains H_2O and O_3 mixing ratios for the time period 1984 to 2022 and data is available for nearly all the stratosphere and parts of the mesosphere. Here, we compare a multi-annual mean of measurements for the years 2013-2016 to two kinds of modeled stratospheric O_3 and H_2O. First, to the EMAC simulations RC1SD-base-10 from Jöckel et al. (2016), with present day meteorology and, second, to HS-sens simulation results. Note that in contrast to the former setup, we are using boundary conditions (RCP6.0) for the year 2050. Hence, CH_4 sources, nitrous oxide, chlorine and bromine source gases differ between the simulations, which in turn causes differences in stratospheric H_2O and O_3 concentrations. While the model setups of RC1SD-base-10 and the one from this publication, HS-sens, are largely the same, we address the differences due to the 2050 boundary conditions for O_3 and H_2O.

2.3.1. SWOOSH introduction and evaluation

The SWOOSH data consists of O_3 and H_2O measured with the satellite Aura MLS and shows no gaps for the years 2013-2016. To compare, Aura MLS measurements of H_2O are quite close to the multi-instrumental mean (MIM), published by the SPARC Data Initiative (Fig. 14, Hegglin et al., 2013, p.11), with a continuous and moderate overestimation at all pressure levels and for both, tropics and extra-tropics. Aura MLS measurements of O_3 agree very well with the MIM at 100-5 hPa and show a small underestimation at 5-1 hPa for both, tropics and mid-latitudes (Fig. 10, Tegtmeier et al., 2013, p.12).

130 We used version 2.6 of the SWOOSH data with a horizontal resolution of 2.5° and 31 vertical levels. The vertical limits are 316-0.002 hPa for H_2O and 261-0.02 hPa for O_3. The vertical resolution of SWOOSH data is 2.5-3.5 km for both, O_3 and H_2O. For the comparison, EMAC data was interpolated to vertical and horizontal levels of SWOOSH data.

2.3.2. EMAC water vapour evaluation

Fig. 11 shows the feature of increasing H_2O mixing ratios with altitude for both, model results and observations. Clearly,
135 observation features are not as homogeneous as model results, but the general agreement is very good. The relative differences show that the magnitude of H_2O mixing ratios in the model setup with present day meteorology is 46±13 % and the HS-sens model setup is 33±8 % smaller than observations on average. The largest differences appear particularly at tropical and southern latitudes in the lower stratosphere.

The increase in average CH_4 mixing ratio of the RCP scenario between the 2010s and 2050s is about 6 %, which increases
140 stratospheric H_2O and could explain the larger difference of observations to RC1SD-base-10 simulations compared to the HS-sens model setup. Note that differences between model and observations should in reality be less than shown in Fig. 11, since H_2O of Aura MLS is slightly overestimated at these altitudes, compared to the MIM of the SPARC Data Initiative. In summary, we conclude that EMAC underestimates the H_2O mixing ratio at stratospheric altitudes for the RC1SD-base-10 results, which are based on trace gas measurements from 2013-2016. For the HS-sens model setup results, which are a projection to 2050,
145 we expect the difference to RC1SD-base-10 to originate mostly from the difference in lower boundary conditions of CH_4.

2.3.3. EMAC ozone evaluation

The multi-annual mean of O_3 shows very good agreement between model and observations (Fig. 12). Clearly, the features look the same and the difference in average magnitude between observation and model is rather small with -5±6 % and -12±6 % for RC1SD-base-10 (present day meteorology) and for the HS-sens model setup (projection to 2050), respectively. For the
150 RC1SD-base-10 scenario SWOOSH observations are within the standard deviation of model simulations. The largest deviations appear in the same areas for both model setups, RC1SD-base-10 and HS-sens. They are at the tropics and southern mid-latitudes at 100 hPa and at polar regions at higher altitudes.

O_3 mixing ratios are expected to increase over time compared to the 2010s, since emission of chlorine and bromine source gases stagnate significantly (World Meteorological Organization et al., 2019; Organization (WMO) et al., 2015). Hence, the
155 difference, when comparing measurements of the 2010s and model results with boundary conditions for the 2050s, is to be expected. Therefore, we conclude that EMAC shows a very good agreement of stratospheric O_3 mixing ratios compared to observations for both HS-sens model results and the RC1SD-base-10 scenario.

2.4. Enhancing the efficient use of computing resources

The simulations with Earth System Models are very time and cost intensive with a high energy consumption. Therefore, we introduce a method, which reduces the number of simulated years of the spin-up phase to three-fifths.

Finite computer resources were mentioned before by Hasselmann et al. (1993) and the related 'cold start' error. The 'cold start' problem refers to coupled atmosphere-ocean simulations that are started close to the present and not early at the beginning of anthropogenic greenhouse gas emission, which eventually generates a significant error in the forcing results due to the too short spin-up phase.

Our computing challenge has an analogy to the above described coupled Atmosphere-Ocean GCM, that are normally run for very long time scales and, therefore have a large reduction potential. Here, we run an Atmospheric-Chemistry GCM for many simulations with variations in the location of emitted trace gases at stratospheric altitudes, each requiring a significant spin-up time (Fig. 3, Pletzer et al., 2022).

With our applied speed-up method, we achieve equilibrium on the multi-annual mean faster and hence are able to reduce the simulated years to two-thirds. The method is the following. We estimate the equilibrium mass change of a species due to an emission and apply an increase of the emissions with a factor s in the first year, so that this equilibrium mass change is approximately reached after a one-year simulation, instead of a 10 year spin-up. The factor s is calculated using a one-dimensional differential equation containing the H_2O perturbation lifetime τ and is therefore depending on altitude (Fig. 13). In a quasi-steady state with a stratospheric H_2O mass perturbation X (kg), an annual emission E (kg/year) and a perturbation lifetime τ (years) we obtain

$$0 = \frac{\delta X}{\delta t} = E - \frac{1}{\tau}X, \qquad (1)$$

or in other words

$$X = \tau E. \qquad (2)$$

To obtain the value of s we solve the differential equation for the evolution of the stratospheric H_2O mass change to Y for an emission sX:

$$\frac{\delta Y}{\delta t} = sE - \frac{1}{\tau}Y, \qquad (3)$$

with the boundary conditions $Y(t = 0) = 0$ and $Y(t = 1) = \tau E$. The solution of the differential equation, that fulfills the first boundary condition is then

$$Y(t) = s\tau E \left(1 - e^{-\frac{1}{\tau}t}\right) \qquad (4)$$

185 In combination with the second boundary condition this gives us

$$s = \frac{1}{1 - e^{-\frac{1}{\tau}}} \qquad (5)$$

Hence, if we estimate s with a Taylor approximation we obtain the perturbation lifetime of τ. However, if we enhance the emission by this factor, we additionally have to consider the loss during the first year with a factor of 0.5, which applies for τ between 2 to 5 years.

190 $$s \approx \tau + 0.5 \qquad (6)$$

We used H_2O perturbation lifetime values at stratospheric altitudes from Grewe and Stenke (2008) and Pletzer et al. (2022) as initial values and inter- and extrapolated to altitudes of 30 km and 38 km, respectively. Since the slope of linear and quadratic extrapolation (35-42 km) were either very steep or too curved we used the average of both values. Using the interpolated τ values we calculated s using Eq. (6).

195 The process during the model runs is as follows. After the first year of simulation, where we enhanced the emissions by the factor s, the initial values of trace gases are emitted for the following years in the simulation. The first year, on one hand, ensures that atmospheric composition changes reach multi-annual equilibrium faster. On the other hand, by limiting the enhancement to the first year, the final mass perturbation is not disturbed, since the atmospheric lifetime of perturbations is shorter than the spin-up phase. For validation, we compared the mass perturbation of H_2O above the tropopause over time for
200 the different scenarios, which is shown in Fig. 14. Please refer to subsection 3.3 for a comparison of scenarios and validation of multi-annual mean equilibrium. To summarize briefly, with the altered spin-up we reduced consumption of normally used computational resources to two-thirds with minimal error potential for all 24 perturbation simulations.

3. Emission scenarios

We use total annual emissions of a potential fleet of hypersonic aircraft that consist of H_2O, NO_x and H_2 emissions. These
205 emissions were presented before by Pletzer et al. (2022) { page 12 } and originate from the 'HIgh speed Key technologies for future Air transport - Research & Innovation cooperation scheme'-project, abbreviated as HIKARI (Blanvillain and Gallic, 2015). H_2O emissions occur as a product of H_2 combustion. Nitrogen oxide is produced at high temperatures during combustion and originate from ambient air (N_2 and O_2). Complete combustion of H_2 is very difficult to achieve and in this dataset it is estimated that 10% of the H_2 fuel remains unburned. These values exclude tropospheric and subsonic emissions and are from

210   altitudes above 18 km, referring to exhaust during cruise phase. The following two subsections contain information on the location and magnitude of all 24 perturbation scenarios.

3.1. Emission locations of perturbation scenarios

The emission scenarios are not based on aircraft route networks, but are box emissions that are varied in latitude and altitude. Altitudes of emission are 30 km and 38 km. Note that the height of the box, where the exhaust is emitted, is approximately 1

215   km. Therefore, it is rather an altitude range with 30-31 km and 38-39 km, where trace gases are emitted. Each latitude region of emission spans 30°. They are southern mid-latitudes at 60-30° S, northern tropics at 0-30° N, northern mid-latitudes at 30-60° N and north polar latitudes at 60-90° N. Clearly, south polar and southern tropics are missing. We refrained from including these two regions for three reasons. First, aircraft barely fly at southern polar regions, since most direct routes between city-pairs do not cross there. Therefore, they are not as important as an emission location. Second, since we included northern

220   tropics, we passed on southern tropics since they show very similar dynamic and chemical conditions in the stratosphere. However, we included southern mid-latitudes to quantify the impact on atmospheric composition and climate on the Southern Hemisphere. Third, with this approach we could reduce the use of computational resources further.
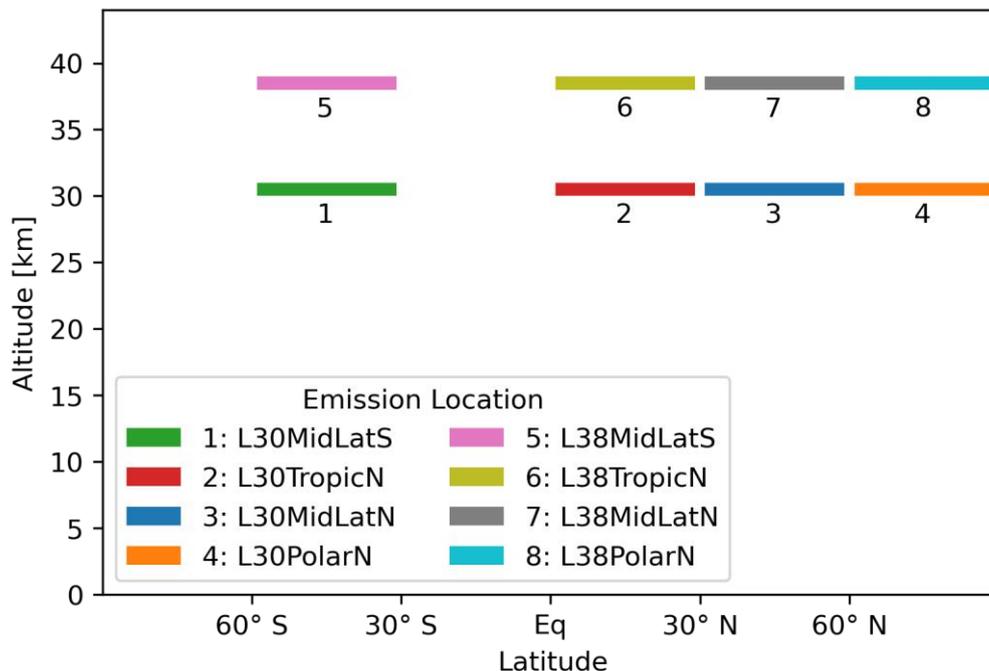
Figure 1: Altitude and latitude region of emission of in total eight emission locations. For three types of emission
225   **these sum to 24 emission scenarios.**

3.2. Emission magnitude of perturbation scenarios

During simulations, the individual trace gases (Table 2) are continuously emitted in the described altitude and latitude regions and with that introduced to physical and chemical processes in the AC-GCM. We aim at identifying the impact on the atmosphere from the cruise phase and hence do not consider other phases such as take-off and landing in this idealized simulation setup.

For each emitted trace gas (H_2O, NO_x, H_2) there are a total of eight simulations, which sum up to 24 simulations in total. The annual magnitude of emitted trace gases is 21.24 teragram of H_2O, 0.031 teragram NO_2 of NO_x and 0.236 teragram of H_2. These values are based on emissions of the aircraft design LAPCAT-PREPHA (Long-Term Advanced Propulsion Concepts and Technologies; Programme de REcherche et de technologie sur la Propulsion Hypersonique Avancée) and are based on approximately 200 flights per day with this aircraft. Why individual emission is appropriate here, even though trace gases are emitted simultaneously during aircraft operation, is discussed in subsection 7.4.

Table 2: Emission scenarios listed by the kind of emission and magnitude.

Emission	Magnitude	Magnitude
H_2O	21.24 Tg/year	1.18 Tmol/year
NO_x	0.031 TgNO$_2$/year	0.67 Gmol/year
H_2	0.236 Tg/year	0.118 Tmol/year

3.3. Timeline and validation

To validate the multi-annual mean equilibrium of atmospheric composition in the context of the speed-up, presented in subsection 2.4, we compare the timeline of H_2O mass perturbations. Of the emitted trace gases H_2O has the longest perturbation lifetime and therefore serves as the medium to verify multi-annual mean equilibrium. Fig. 14 shows the temporal evolution of H_2O mass perturbation. Three phases can be seen. (1) The first year shows a sharp increase due to the applied speed-up factor s (gray shaded area). (2) From 2008-2012, some scenarios overshot equilibrium values with the end of the first year, e.g. 30 km, 60-90°N, and level off to equilibrium values. Other scenarios continue to build up, e.g. most scenarios at 38 km, before reaching equilibrium (green shaded) latest in 2013 (3).

The different behavior most probably originates from latitudinal differences in H_2O perturbation lifetime, which were not included in the inter- and extrapolation in subsection 2.4. The error potential should not be significant, since the time to equilibrate is sufficient for all scenarios and multi-annual mean equilibrium is reached latest in 2013. Clearly, equilibrium is not reached within one year as assumed and total spin-up until equilibrium amounts to 6 years, since latitudinal differences had to be taken into account as well. However, without the spin-up method, we would require 10 years (Fig. 3, Pletzer et al., 2022) and hence we could reduce the spin-up computing time by 40 % and total computing time by approximately 33 %.

4. Atmospheric composition changes

In this section we present, first, as an overview of simulation results, i.e. the impact on the two most important climate active gases in the context of hypersonic aircraft exhaust, O_3 and H_2O, and, second, direct and indirect effects on atmospheric composition by the emission of H_2O, NO_x and H_2 for all 24 scenarios. Third, we address CH_4 and H_2O perturbation lifetime. Note that all presented data in this section is based on multi-annual mean model results with both, specified meteorology (2013-2016) and 2050 source gas emissions.
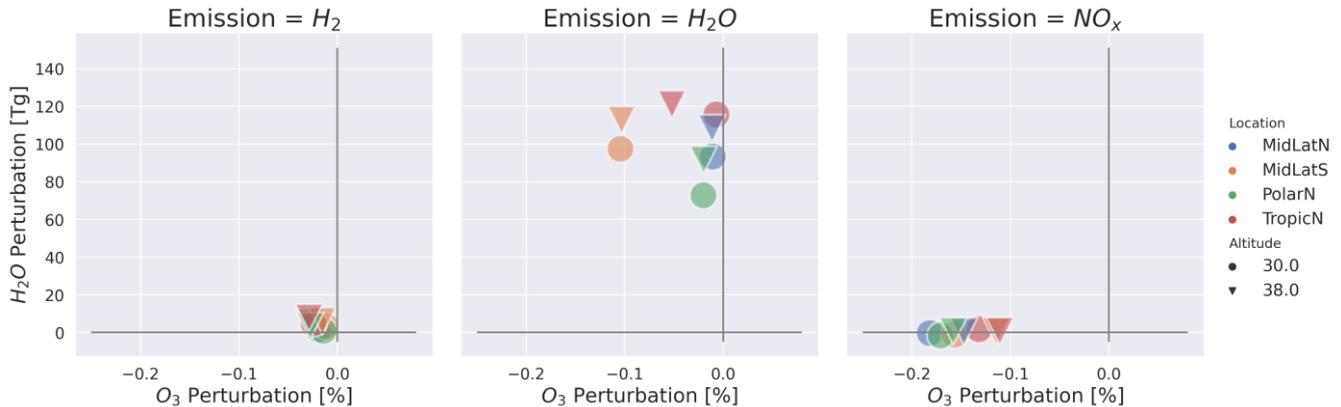
Figure 2: Overview of H_2O and O_3 changes for all 24 simulations grouped by initial emission of H_2, H_2O and NO_x (left, middle, right). Colours refer to the latitude region of emission (southern mid-latitudes, northern tropical latitudes, northern mid-latitudes, north polar latitudes) and markers to altitude of emission. Please refer to Table 4 for statistical significance.

Fig. 2 shows the H_2O mass perturbation and relative O_3 changes above the meteorological tropopause (WMO) grouped by emitted species. Hydrogen (H_2) emission has a comparably small effect on both, H_2O and O_3. Relative O_3 changes range from -0.01 % to -0.03 %, with a decrease for all H_2 emission scenarios. The effect is larger for the higher altitude scenarios. H_2O changes are not larger than 8 Tg, with maximum values for the northern tropic emission scenario at 38 km. H_2O emission has a large effect on H_2O mass perturbation in all scenarios with a range of 73-121 Tg. Values for higher altitude and lower latitude scenarios are particularly large. Relative O_3 change is rather small, except in the southern mid-latitudes where O_3 depletion is approximately 0.1% for both altitudes. The altitude of emission has a large effect for emission at the tropics and emission at 38 km has a significantly larger impact on ozone. NO_x emission has the lowest effect on H_2O mass perturbation. The range of H_2O changes is -1.6 to 1.7 Tg and all higher altitude emission scenarios show an increase with medium values. In contrast, the lower altitude emission scenarios show larger values, but differ in increase and decrease. Relative O_3 change due to NO_x emission is larger than most other emission scenarios with a range of -0.11 to -0.18 %. Largest values appear at northern mid-latitudes and polar regions at 30 km.

275 The following subsections are further divided in 'Direct Effects' and 'Indirect Effects'. The former relates to the emission and its effect on the same molecular atmospheric compound, e.g. H_2O emission on H_2O trace gas concentrations. The latter includes indirect effects on other atmospheric compounds like CH_4 or O_3. The shaded box in each subfigure represents the altitude of emission. Hatched areas represent a p-value larger than written in the title of each subplot (Table 3).

Table 3: Markers for probability levels of significance test

Probability	$p \gtrless 0.05$	$p \gtrless 0.01$	$p \gtrless 0.001$
Marker	*	**	***

4.1. Water vapour emission

4.1.1. Direct effects

Fig. 3 shows the H_2O perturbation in parts per million volume for the H_2O emission scenarios. When comparing the altitudes 38 km and 30 km, which are the first and second line, respectively, the H_2O mixing ratios are generally higher for the former. H_2O emissions at low latitudes are distributed across both hemispheres. H_2O emissions at higher altitudes are to a significantly

285 larger extent confined to one hemisphere. The threshold for failing the t-test is exceeded at and below the tropopause region.
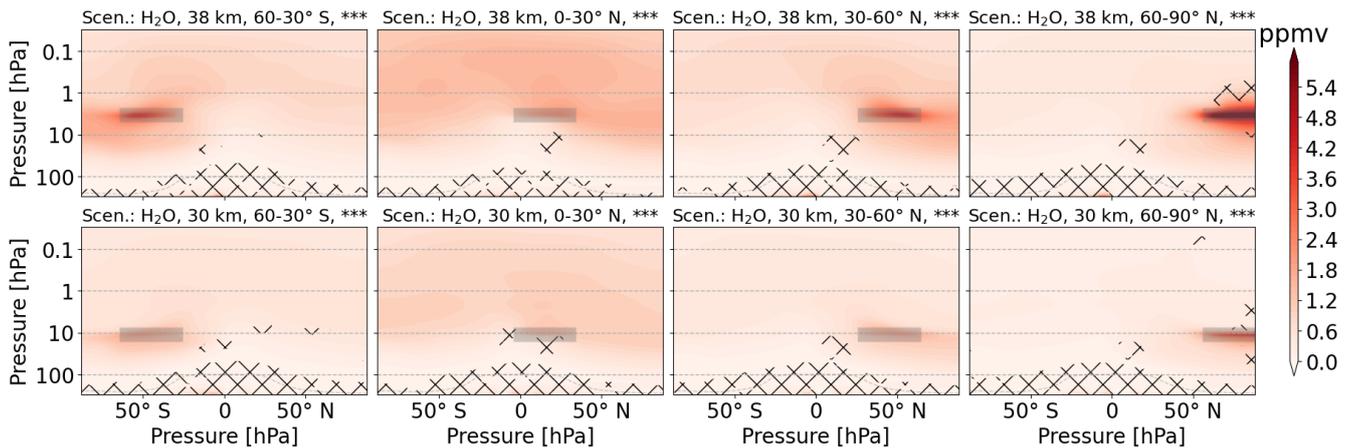
Figure 3: Zonal mean of H_2O perturbation (volume mixing ratio, ppmv) for scenarios where H_2O is emitted. The first and second row refer to 38 km and 30 km altitude of emission, respectively. Columns represent the latitude region of emission. The emission regions are shaded in grey. Lines indicate statistical insignificant results and the probability
290 **level is written in the title of each subplot.**

4.1.2. Indirect effects

4.1.2.1. Ozone

In total, the H_2O emission causes O_3 depletion, especially at southern latitudes (Fig. 2). In Fig. 4 the O_3 perturbation (volume mixing ratio) is divided into layers of O_3 decrease (above 3 hPa and below 10 hPa) and O_3 increase (3-10 hPa) in all subfigures. For emission at 38 km, the upper layer of O_3 decrease seems to be strengthened. For emission at 30 km, the layer of O_3 increase overlaps with the emission region and seems to be weakened, especially for H_2O emission from 0-30° N. The threshold for failing the t-test has in general a large variation and appears at the interface of O_3 increase and O_3 decrease regions, the tropopause and polar regions. The largest values of O_3 increase is situated in the tropics for all scenarios. In contrast, the largest values of O_3 decrease move with the emission location.
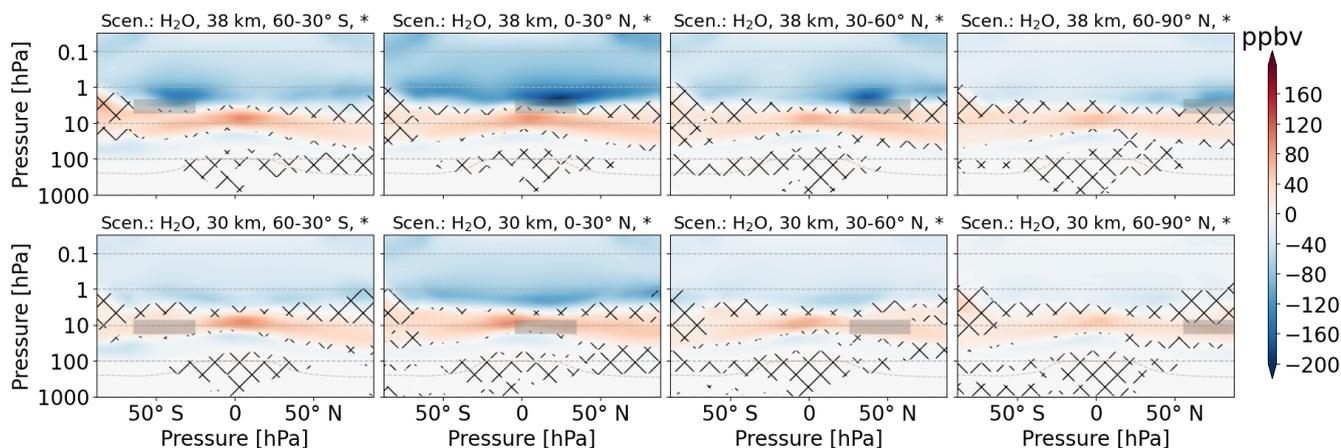
Figure 4: Zonal mean of O_3 perturbation (volume mixing ratio, ppbv) for scenarios where H_2O is emitted. The first and second row refer to 38 km and 30 km altitude of emission, respectively. Columns represent the latitude region of emission. The emission regions are shaded in grey. Lines indicate statistical insignificant results and the probability level is written in the title of each subplot.

4.1.2.2. Hydrogen

The H_2O emission has a significant effect on H_2 (Fig. 17) at the top of the modelled atmosphere (around 80 km). In general, the H_2 perturbation patterns are very similar with a broad layer at high latitudes and smaller width at mid to low latitudes. The magnitude, however, is larger for emission scenarios with low latitudes and the higher emission altitude (38 km).

4.1.2.3. Methane

The impact of H_2O emission on CH_4 shows complex patterns, with areas of increase and decrease, and the multi-annual variability is clearly large, since the t-test restricts confidence in many areas (Fig. 5). It is common knowledge, that OH oxidizes CH_4 and adds to H_2O concentrations in the stratosphere. Additionally, it was shown, that emission of H_2O eventually increases CH_4 oxidation (Pletzer et al., 2022). Overall, H_2O emissions reduce CH_4 concentrations the most compared to emissions of

NO_x and H_2 (that changes when normalized to the number of emitted molecules). The features for emission at southern mid-latitudes are very similar with a decrease from 100-10 hPa and an additional decrease around the emission location of the higher altitude scenario. H_2O emission at northern tropics causes a wide-spread CH_4 depletion with a larger impact for the higher altitude emission. A CH_4 increase is visible in the tropics at 10 hPa for 30 km emission. For 38 km, the area with CH_4 increase, where $p \gtrsim 0.05$, is barely visible. Northern mid-latitude emission of H_2O shows features similar to southern mid-latitude emission, but the decrease is at slightly higher altitudes. Areas of increase and decrease seem to have switched location. This statement should be taken with caution, since not all areas, included in the comparison, fulfil the t-test criteria, i.e. the error probability that means are not different is larger than 5 %. North polar emission scenarios are very similar to the north mid-latitude emission scenarios. However, perturbations of volume mixing ratios are generally smaller.
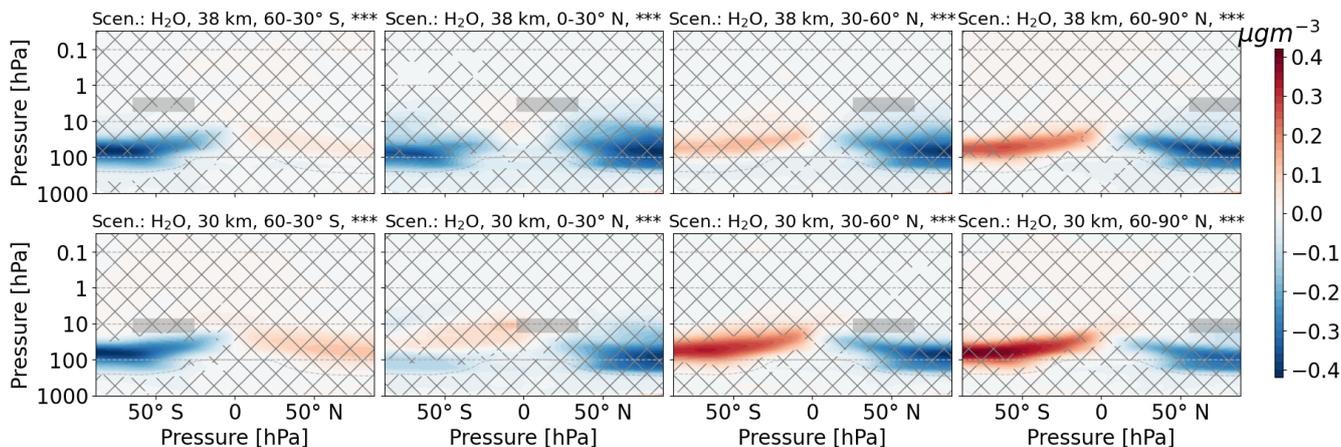
Figure 5: Zonal mean of CH₄ perturbation (volume mixing ratio, ppbv) for scenarios where H₂O is emitted. The first and second row refer to 38 km and 30 km altitude of emission, respectively. Columns represent the latitude region of emission. The emission regions are shaded in grey. Lines indicate statistical insignificant results and the probability level is written in the title of each subplot.

4.2. Nitrogen oxide emission and ozone perturbation

4.2.1. Direct effects

The emitted NO_x is, compared to H_2O, more confined to the emission region. First, the NO_x perturbation maximum is clearly located at the altitude and latitude of emission — other maxima are not visible. Second, the multi-annual mean of emission scenarios and the reference scenario are different for most areas in direct proximity to the emission location (hatched area). NO_x changes are more distributed for low latitude emission scenarios. The vertical distribution shows downward transport for high latitudes and upward transport for low latitudes, depending on latitude of emission. A correlation plot of significant NO_x and O_3 changes (Fig. 19) shows a nearly linear correlation for altitudes from the surface to 4 hPa with a tendency to saturation for larger NO_x perturbations in the lower altitude emission scenarios. For altitudes from 4-0.01 hPa the correlation is curvilinear

and the NO_x emission scenarios show a larger range of values, compared to the lower altitude range. Here, the sensitivity is very large to the altitude and latitude of emission.

Since the correlation of O_3 and NO_x perturbation is well known, we include the O_3 perturbation as a 'direct' effect. When comparing Fig. 20 and Fig. 6 the similarity is clearly visible. Areas of NO_x increase overlap with areas of O_3 decrease. Additionally, we see areas of O_3 increase below areas of O_3 decrease at southern mid-latitude and northern tropic emission scenarios. Note that the magnitude is much smaller and results are clearly significant. For northern mid-latitude scenarios, these are barely visible in the tropics and for north polar emission scenarios they are not visible.
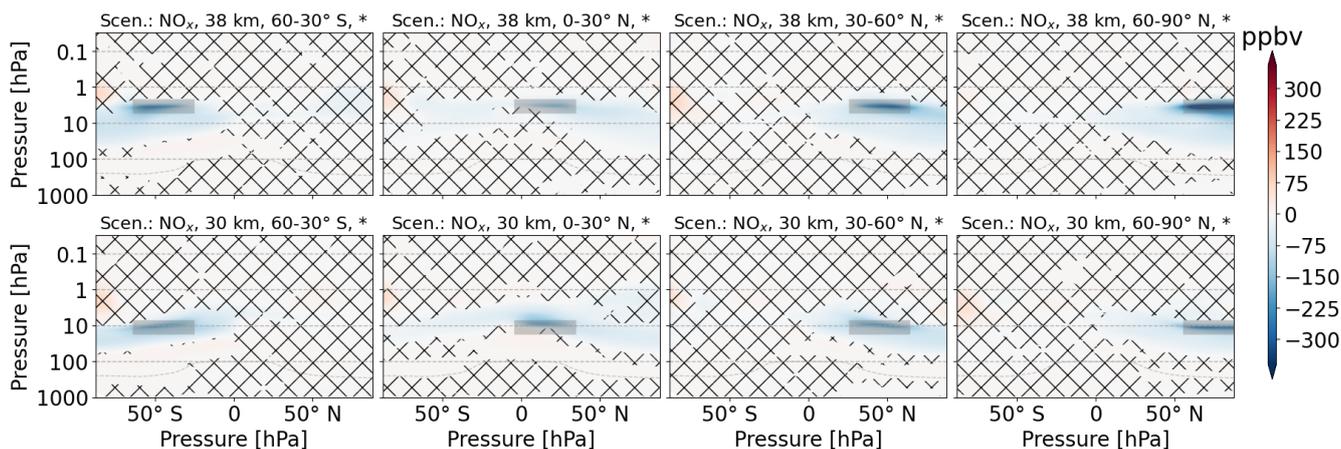
Figure 6: Zonal mean of O_3 perturbation (volume mixing ratio, ppbv) for scenarios where NO_x is emitted. The first and second row refer to 38 km and 30 km altitude of emission, respectively. Columns represent the latitude region of emission. The emission regions are shaded in grey. Lines indicate statistical insignificant results and the probability level is written in the title of each subplot.

4.2.2. Indirect effects

Overall, indirect effects of NO_x emission on H_2O, H_2 and CH_4 are basically insignificant for most areas. For some scenarios, significant areas appear for tropospheric and lower stratospheric altitudes, largely depending on which hemisphere NO_x was emitted (Fig. 21, Fig. 22, Fig. 23).

4.3. Hydrogen emission

4.3.1. Direct effects

The increase in atmospheric concentrations of H_2 by H_2 emission peaks at the emission location (Fig. 7). The perturbation pattern looks very similar to H_2O perturbation from H_2O emission and is therefore most probably dominated by transport, i.e. the Brewer-Dobson circulation, instead of photochemistry.
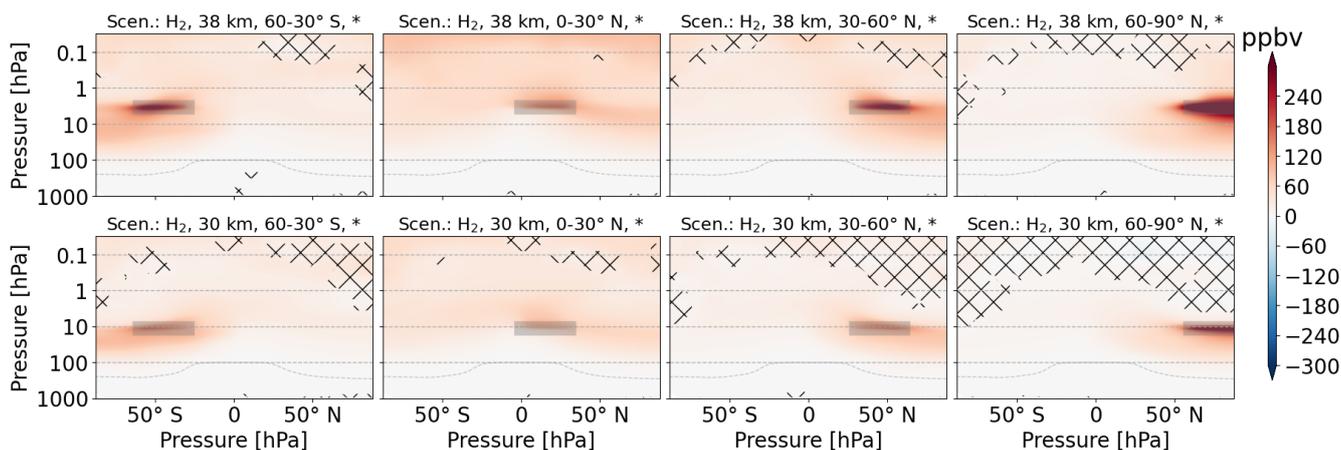
Figure 7: Zonal mean of H$_2$ perturbation (volume mixing ratio, ppbv) for scenarios where H$_2$ is emitted. The first and second row refer to 38 km and 30 km altitude of emission, respectively. Columns represent the latitude region of emission. The emission regions are shaded in grey. Lines indicate statistical insignificant results and the probability level is written in the title of each subplot.

4.3.2. Indirect effects

The EMAC results show that H$_2$ emissions at 38 km generally and for the tropics at 30 km statistically significant reduce the O$_3$ abundance in the upper stratosphere (0.1-1 hPa). It is known that above 40 km the HOx cycle starts to dominate the O$_3$ depletion instead of the NO$_x$ cycle (Zhang et al., 2021a; Matthes et al., 2022).

Maximum values of H$_2$O perturbation are approximately 5 % of the H$_2$O perturbation of the direct H$_2$O emission scenarios. Apart from the magnitude, the features are very similar, which again suggests that transport dominates these perturbations (Fig. 25). Largest perturbations appear for the higher altitude scenarios and the low latitude scenarios. A correlation plot shows that statistically significant H$_2$O changes due to H$_2$ emission show different orders of magnitude depending on Hemisphere with larger gradients appearing rather in the Southern Hemisphere. Clearly, high latitude and low altitude emission scenarios show smaller H$_2$O changes and again suggests a dominant role of transport for the perturbation lifetime.

CH$_4$ perturbation patterns are mostly not statistically significant (Fig. 26).

4.4. Methane, water vapour perturbation lifetime and overview of relative changes

4.4.1. Methane and methane lifetime

Tropospheric and whole model domain CH$_4$ lifetime of all emission scenarios is 8.39 and 9.54 years on average, respectively. We used the following equation to calculate both, the tropospheric and whole domain CH$_4$ lifetime τ_{CH4}.

$$\tau_{CH_4}(t) = \frac{\sum_{b \epsilon B} M^b_{CH_4}(t)}{\sum_{b \epsilon B} k^b_{CH_4}(t) \cdot [OH]^b(t) \cdot M^b_{CH_4}(t)} \qquad (7)$$

$M^b_{CH_4}$ is the CH_4 mass, $[OH]^b$ the concentration and $k^b_{CH_4}$ the reaction rate of CH_4 + OH in grid box b. B is the set of all grid boxes.

Eq. (7) was applied to calculate the tropospheric CH_4 lifetime for different EMAC model setups (Fig. 16, Jöckel et al., 2016). The results show an average value over all setups of 8.0±0.6 for the years 2000-2004, which, according to the authors, is on the lower end of a set of values from other publications.

Fig. 15 shows the CH_4 lifetime (a) and H_2O mass perturbation (b) in relation to the relative hydroxyl radical mass change. CH_4 lifetime changes of H_2 emission scenarios are quite close to the reference scenario and a clear trend is not visible. H_2O emission scenarios show a clear correlation between OH increase and CH_4 lifetime decrease, with an increase or only small change at higher northern latitude and lower altitude scenarios and a decrease of CH_4 lifetime for southern and tropical latitude scenarios (Table 4). An average over all emission scenarios per emission type shows an increase of relative hydroxyl and hydroperoxyl mass mostly in the middle atmosphere (Table 7). This explains the decreasing global CH_4 lifetime for H_2O with a more efficient CH_4 oxidation due to an increase in OH (Fig. 15 (b)).

NO_x emission scenarios, which show small OH perturbations close to zero, also show the largest reduction in τ_{CH4} with two altitude clusters (green shaded ellipses). As an addition, Fig. 16 in the appendix shows the tropospheric CH_4 lifetime, which shows very similar trends for NO_x emission scenarios compared to the whole model domain CH_4 lifetime. According to literature two pathways of tropospheric chemistry connect NO_x and OH concentrations. On one hand, HO_2 to OH recycling is speed-up by NO and eventually increases OH. On the other hand, NO_2 oxidation reduces OH concentrations and increases nitric acid (HNO_3) concentrations (Ehhalt et al., 2015, p.p. 245). Note that tropospheric OH concentrations are only slightly increased for NO_x emission scenarios (Table 7). The above-mentioned processes might not allow large perturbations of OH to build up, even though the effect on CH_4 lifetime are the largest in all scenarios.

In the troposphere, H_2O emission and NO_x emission scenarios show an inverse trend with a tropospheric CH_4 lifetime increase (Fig. 16,) combined with tropospheric hydroxyl decrease (Table 7) for the former and tropospheric CH_4 lifetime decrease combined with tropospheric hydroxyl increase for the latter. In summary, the important processes for global CH_4 lifetime take place in the troposphere for NO_x scenarios and in the middle atmosphere for H_2O emission scenarios.

4.4.2. Water vapour perturbation lifetime

Fig. 8 shows an increase in H_2O perturbation lifetime with altitude. Values at tropospheric altitudes range from approximately 1 hour to half a year. Generally, the H_2O perturbation lifetime is longest at tropical regions and high altitudes and gets less at

higher latitudes and lower altitudes. The lifetime range at stratospheric altitudes is large from 1 month to 5.5 years, which includes the extension that is based on this work. We used our data to extend the altitude dependency of H_2O perturbation lifetime in existing literature to higher altitudes. Grewe and Stenke (2008) published H_2O perturbation lifetime from the surface to approximately 20 km (50 hPa). We extended the range up to approximately 40 km (3 hPa). The transport of low latitude

410 high altitude H_2O emissions to the high latitudes of the troposphere along the shallow and deep branches of the Brewer-Dobson circulation takes the longest time. Hence, transport of H_2O perturbations dominates the perturbation lifetime for both, the previous and the extended altitudes. Pletzer et al. (2022) showed that photochemistry does not reduce total H_2O perturbations at 26 and 35 km cruise altitude. We report that perturbation lifetimes continues to increase with altitude for all latitudes and that photochemistry does not deplete total H_2O perturbations for emissions up to 38 km.
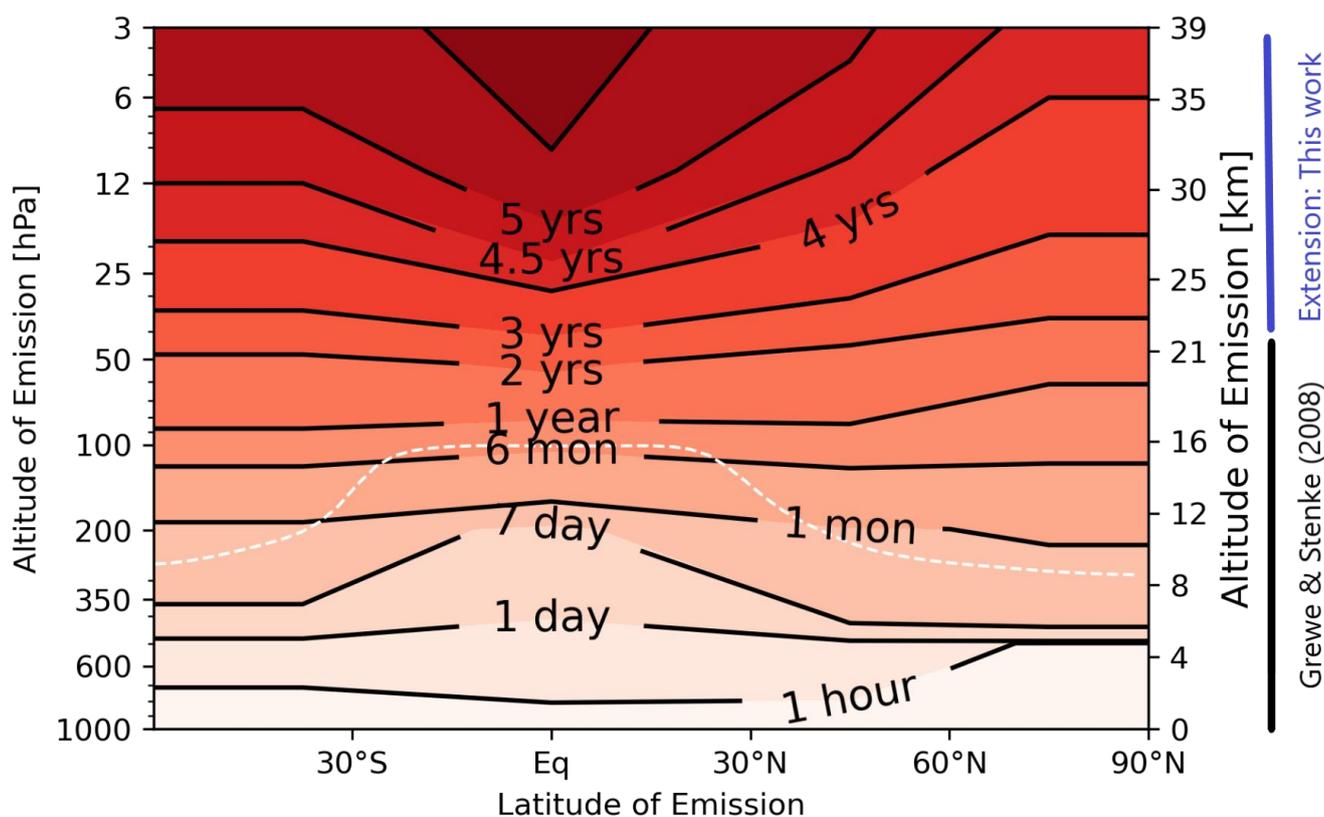
415

Figure 8: Reproduced from Grewe and Stenke (2008), Fig. 6 (a), with permission from the authors, who provided the data. The figure shows the water vapour perturbation lifetime for the original pressure levels (1000-52 hPa) and the extended pressure levels (52-3 hPa) depending on latitude. The vertical regions are marked next to the right y-axis with black and blue lines, respectively.

4.4.3. Overview on atmospheric composition

For a quick-look overview of sensitivities, we present Table 4, which shows the effect of one gigamole or teramole of H_2O, NO_x and H_2 emission on H_2O (above the tropopause), whole model domain O_3 and whole model domain CH_4 lifetime τ_{CH4}. We added background colours blue, yellow and green, indicating that the values differ from zero with a probability of 95 %, 99.9 % and 99.99 %. The impact of NO_x, H_2O and H_2 emission on O_3 is statistically significant with 99.99 % confidence for all 24 sensitivities. For sensitivities of H_2O and CH_4 lifetime, 13 and 8 out of 24 means are different to the reference with at least 95 % confidence, respectively.

Sensitivity of Atmospheric Composition Changes to Emission of NO_x, H_2O and H_2

Emission	Altitude	ΔH₂O (above tropopause, WMO)				Unit	ΔO₃ (Whole Model Domain)				Unit	Δτ_CH4 (Whole Model Domain)				Unit
1 Gmol NOx	30 km	-0,09	0,14	-0,03	-0,13	Tmol	-0,17	-0,14	-0,20	-0,18	Tmol	-0,14	-0,15	-0,15	-0,16	%
	38 km	0,07	0,06	0,04	0,05	Tmol	-0,12	-0,12	-0,16	-0,17	Tmol	-0,06	-0,06	-0,12	-0,11	%
1 Tmol H₂O	30 km	4,58	5,44	4,39	3,42	Tmol	-6,43	-0,42	-0,64	-1,23	$\times 10^{-2}$ Tmol	-22,2	-19,2	14,3	21,0	x 10-3 %
	38 km	5,31	5,70	5,10	4,31	Tmol	-6,36	-3,21	-0,69	-1,22	$\times 10^{-2}$ Tmol	-29,6	-41,9	1,2	-2,1	x 10-3 %
1 Tmol H₂	30 km	1,56	2,35	0,81	0,44	Tmol	-7,4	-15,1	-12,2	-8,7	$\times 10^{-2}$ Tmol	10,9	0,9	-12,6	-0,8	x 10-2 %
	38 km	2,86	3,69	2,45	1,62	Tmol	-9,5	-17,9	-16,6	-17,1	$\times 10^{-2}$ Tmol	1,5	-12,0	-10,7	4,1	x 10-2 %
	Latitude	60-30° S	0-30° N	30-60° N	60-90° N		60-30° S	0-30° N	30-60° N	60-90° N		60-30° S	0-30° N	30-60° N	60-90° N	

*** ** *

Table 4: Sensitivities of atmospheric composition changes, water vapour in teramole (ΔH₂O), relative ozone change in teramole (ΔO₃) and relative change of whole model domain methane lifetime (Δτ$_{CH4}$), to emission of H_2O, NO_x and H_2 depending on altitude and latitude of emission. Asterisk refer to statistical significance (Table 3).

4.4.3.1. Water vapour perturbation in the middle atmosphere

The term stratospheric H_2O is quite common. Since the HS-sens model setup includes parts of the mesosphere, we prefer to use the term mid-atmospheric H_2O. For H_2O emission, the sensitivity of mid-atmospheric H_2O increases clearly with altitude and is higher for lower latitude emission scenarios, which is also shown in Fig. 8. The impact of H_2 emission on mid-atmospheric H_2O is very similar and increases with altitude and is larger for lower latitudes. The order of magnitude of changes per molecule of emitted species shows that a molecule of H_2 is roughly 50 % as effective in enhancing the mid-atmospheric H_2O concentration as a molecule of emitted H_2O (Table 4). The relevant reactions include both, loss and production of H_2O. Chemically, the production is initiated directly by reaction $H_2 + OH \rightarrow H_2O + H$ and indirectly by $HO_2 + OH \rightarrow H_2O + O_2$. The latter is facilitated by the general increase of HO_x and included in a H_2O-HO_x cycle via reaction $H_2O + O(^1D) = 2\,OH$. Increased oxidation, e.g. methane and nitric acid oxidation, contributes a small amount as well. The net production of H_2O briefly discussed in subsection 7.2.

4.4.3.2. Whole model domain ozone perturbation

Generally, all three types of emissions cause O_3 depletion. However, the effect of NO_x emission on whole model domain O_3 is two and three orders of magnitude larger compared to H_2 and H_2O emission, respectively. Hence, a NO_x molecule is roughly 3 to 4 orders of magnitude more efficient in reducing the stratospheric O_3 burden than H_2 or H_2O. Interestingly, while in absolute values the H_2 emissions are of minor importance to the O_3 depletion, the average effectiveness in destroying O_3 is roughly 5-6 times larger for H_2 than for H_2O (Table 4).

4.4.3.3. Whole model domain methane lifetime change

The number of significant results of CH_4 lifetime changes is low compared to atmospheric sensitivities of H_2O or O_3. CH_4 lifetime changes of NO_x emission scenarios are lower at the higher altitude and show ranges between -0.06 to -0.16 % per Gmol of NO_x emission. Per molecule CH_4 lifetime changes of H_2O emission scenarios are four to five orders of magnitude smaller than compared to NO_x emission scenarios. Note that CH_4 lifetime in H_2O and NO_x emission scenarios clearly shows a linear trend or clusters depending on altitude respectively, while H_2 emission scenarios do not show a clear trend (Fig. 15).

5. Radiative forcing

We used the atmospheric changes of the radiatively active gases, H_2O, O_3 and CH_4, to calculate the stratospheric-adjusted radiative forcing (total net RF) at the tropopause (about 180 hPa).

In Fig. 9, we present the total net RF, which shows the total shortwave (SW), total longwave (LW) and total net RF grouped by emission and aligned by latitude and marked by altitude of emission. Here, 'total' refers to the combined effect of RF due to H_2O, O_3 and CH_4 changes. In the following subsections, we address the individual, H_2O, O_3, CH_4 altitude and latitude dependencies of RF and the relation of RF to atmospheric composition changes.
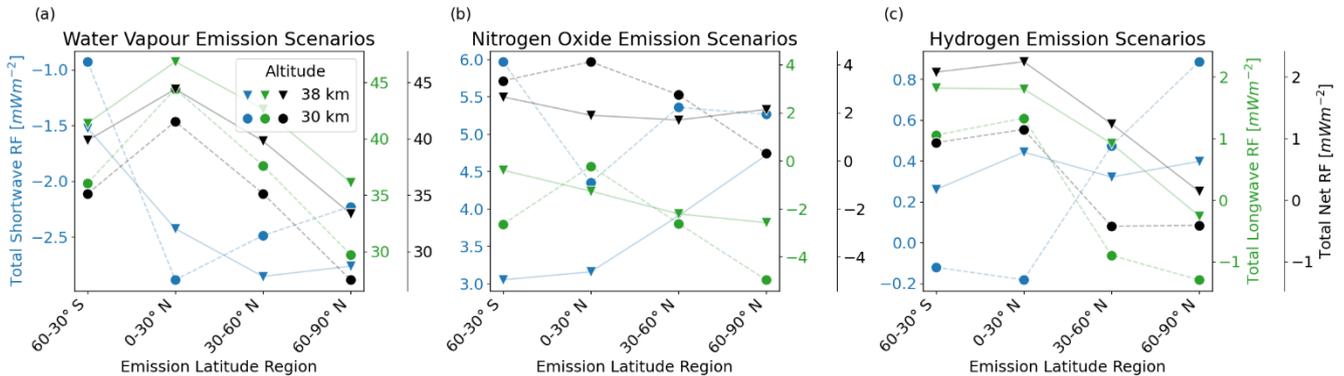
Figure 9: The total shortwave, longwave and net radiative forcing in blue, green and black, respectively, for water vapour (a), nitrogen oxide (b) and hydrogen (c) emission scenarios due to atmospheric composition changes of water

vapour, ozone and methane. For different altitude emission scenarios refer to markers. Latitude regions of emission are aligned on the x-axis.

Comparing the magnitude, the H_2O emission scenarios show the largest total net RF, followed by NO_x and H_2 emission scenarios.

H_2O emission scenarios all have a negative total SW RF (blue), which is smallest at southern mid-latitudes. The total LW RF (green) is largest for tropical, and smallest for the north polar emission scenarios. The high altitude emission scenarios show a larger total LW RF for all latitudes.

NO_x emission scenarios show a positive total SW RF, which is larger for the lower altitude scenarios. In comparison, the total LW RF is negative and smaller, with no distinctive altitude dependency.

H_2 emission scenarios have a positive total SW RF, apart from the lower altitude emission scenarios at southern mit-latitudes and the tropics. The total LW RF clearly depends on altitude with larger values for the high altitude emission scenarios, the Southern Hemisphere and the northern tropics.

5.1. Water vapour radiative forcing

H_2O emission scenarios have the largest radiative forcing of the emission scenarios, followed by H_2 and NO_x emission scenarios. Fig. 28 shows the H_2O SW RF, H_2O LW RF and H_2O net RF due to H_2O changes.

For H_2O emission scenarios the H_2O SW RF has the largest negative values for emission in the tropics and the lowest negative values for emission at north polar latitudes. The H_2O LW RF shows the inverse trend with largest positive values for emission in the tropics and lowest positive values for emission at north polar latitudes. Overall, H_2O LW RF dominates the H_2O net RF.

For NO_x emission scenarios the H_2O SW RF is mostly positive, whereas the H_2O LW RF is negative. The H_2O net RF is negative apart from the emission at 30 km in the tropics.

For H_2 emission scenarios the H_2O SW RF is negative for emission at southern mid-latitudes and the tropics and positive for emission at most northern mid-latitudes and at the northernmost latitudes. The H_2O LW RF shows the inverse trend with warming at southern mid-latitude and tropic emission and cooling only for emission at the lower altitudes for northern mid- and high-latitudes. The LW RF dominates the net RF by an order of magnitude.

5.2. Ozone radiative forcing

Fig. 29 is based on O_3 changes, excluding H_2O and CH_4 changes. For H_2O emission scenarios the O_3 SW RF is positive with maximum values of 1.75 mWm^{-2} for southern latitude emission and continuously becomes close to zero the further north H_2O is emitted. The O_3 LW RF shows an inverted trend with large negative values for emission at southern latitudes and values

between 0 and -1 mWm^{-2} for other emission locations. The altitude dependency of O_3 SW RF is largest for emission at tropical regions and, in contrast, O_3 LW RF shows larger altitude differences only at higher latitude emission scenarios. Overall, there is a clear altitude distinction of net O_3 RF due to H_2O emission and values are negative and positive.

For H_2 emission scenarios the O_3 SW RF shows only a small latitude dependency around 0.4 mWm^{-2} for the higher altitude emission scenarios. In contrast, the lower altitude emission causes negative values up to -0.2 mWm^{-2} for emission at southern latitudes to the tropics and has positive values for north polar emission. The O_3 LW RF is negative and differences of high and low altitude emission are largest for emission at the tropics. Since O_3 LW and SW RF tend to cancel each other, the net O_3 RF has generally lower values than the individual contributions and we report a stronger cooling by O_3 perturbation due to H_2 emission for the lower altitude at all latitude emission scenarios except north mid-latitude and north polar emission.

5.3. Methane radiative forcing

CH_4 composition changes contribute significantly less to RF than atmospheric composition changes of H_2O and O_3. The range of CH_4 net RF is -0.17 to 0.05 mWm^{-2} and LW RF is larger than SW RF in many scenarios (Fig. 30).

For H_2O emission scenarios the CH_4 net RF cools more for the higher altitude scenarios. For lower altitude scenarios radiation flux changes are smaller, apart for northern mid-latitude emission with an effect close to zero and north polar emission with a comparably small heating.

The NO_x emission scenarios show a warming for the lower altitudes scenarios, apart for emission at southern latitudes, for which a comparably larger cooling effect occurs. For higher altitude emission scenarios the CH_4 net RF is close to zero for southern mid-latitude and tropic emission and cools for northern mid-latitude and north polar emission of NO_x.

H_2 emission scenarios show both warming and cooling with LW and SW due to the CH_4 perturbation. A continuous cooling appears for the higher altitude emission scenarios. The lower altitude emission scenarios show alternating values of warming and cooling depending on latitude.

5.4. Individual radiative forcing and the related perturbations

5.4.1. H_2O net radiative forcing

The average sensitivity of H_2O net RF to one teragram of H_2O increase is 0.37±0.01 mW m^{-2} (TgH$_2$O)$^{-1}$ for H_2O emission scenarios, 0.10±0.79 mW m^{-2} (TgH$_2$O)$^{-1}$ for NO_x emission scenarios and 0.14±0.28 mW m^{-2} (TgH$_2$O)$^{-1}$ for H_2 emission scenarios. The standard deviation, i.e. latitude and altitude variation, is large for the latter two and only H_2O emission scenarios always result in a radiative warming with a low standard deviation.

520 Fig. 31 shows the relation of H_2O net RF and H_2O perturbation above the tropopause for all emission scenarios. The relation increases linearly for low values of H_2O perturbation, with slight underestimate of NO_x and H_2 emission scenarios. The results confirm the linear relation between stratospheric H_2O perturbations and RF from earlier findings and for lower emission altitudes (dashed gray line, (Fig. 8, Grewe et al., 2014a)). However, for higher perturbations deviations in RF appear and the relation $\frac{\Delta RF}{\Delta H_2O}$ continuous to decrease. A two dimensional polynomial fit captures the data points well with very small

525 deviations.

5.4.2. O_3 net radiative forcing

The average sensitivity of O_3 net RF to one percent of O_3 decrease is -9.9 ± 38.2 mW m^{-2} (%O_3)$^{-1}$ for H_2O emission scenarios, 20.2 ± 6.1 mW m^{-2} (%O_3)$^{-1}$ for NO_x emission scenarios and -7.4 ± 8.7 mW m^{-2} (%O_3)$^{-1}$ for H_2 emission scenarios. The interannual variability is particularly large for H_2O emission scenarios. For the NO_x emission scenarios, O_3 decrease always causes

530 warming.

Fig. 32 shows the relation of O_3 net RF to relative O_3 change for all emission scenarios. The NO_x emission scenarios are clustered and the related O_3 depletion causes warming. For the lower altitude scenarios, different levels of O_3 decrease do not cause a large difference in warming. In contrast, for higher altitude scenarios the latitude of emission has a larger impact on both O_3 depletion and O_3 net RF variability. H_2O and H_2 emission scenarios are clustered around close to zero RF, apart from

535 three single H_2O emission scenario values, where the pair is emission at southern mid-latitudes and the single value at northern tropics. The comparably large O_3 depletion for H_2O emission at southern mid-latitudes originates from enhanced denitrification by increased H_2O concentrations within polar stratospheric clouds (not shown), which is known to be stronger in southern polar regions compared to northern polar regions (Tabazadeh et al., 2000).

5.4.3. CH_4 net radiative forcing

540 The average sensitivity of CH_4 net RF to one percent of global CH_4 decrease is -8.7 ± 10.2 mW m^{-2}/% CH_4 for H_2O emission scenarios, -39.5 ± 88.1 mW m^{-2}/% CH_4 for NO_x emission scenarios and 2.1 ± 35 mW m^{-2}/% CH_4 for H_2 emission scenarios. Clearly, the spread is large.

All of NO_x and H_2 emission scenarios are clustered around zero RF, with both radiative warming and cooling (Fig. 33). H_2O emission scenarios show warming, no change and cooling for the lower altitude emission. For higher altitude emission the

545 larger CH_4 reduction comes with a cooling effect. Both altitudes combined scale approximately linear, however the line crosses from cooling to warming slightly below the inversion of CH_4 decrease to CH_4 increase.

5.4.4. Summary on radiation

Emission		Sensitivity of Radiative Forcing caused by Atmospheric Composititon Changes to Emission of NO_x, H_2O and H_2														
	Altitude	ΔH_2O net RF				Unit	ΔO_3 net RF				Unit	ΔCH_4 net RF				Unit
1 Gmol NOx	30 km	-0,54	1,20	0,05	-1,02	mWm^{-2}	5,84	5,98	4,21	3,22	mWm^{-2}	0,009	0,028	0,023	0,021	mWm^{-2}
	38 km	0,84	0,45	0,57	0,43	mWm^{-2}	4,73	2,22	3,08	3,42	mWm^{-2}	0,018	0,028	-0,020	-0,022	mWm^{-2}
1 Tmol H2O	30 km	30,66	34,19	29,74	24,07	mWm^{-2}	-3,60	-1,49	-2,14	-2,15	mWm^{-2}	0,016	0,005	0,028	0,010	mWm^{-2}
	38 km	34,09	35,59	32,78	28,67	mWm^{-2}	-3,38	-1,28	-1,66	-2,30	mWm^{-2}	0,012	-0,005	-0,003	-0,018	mWm^{-2}
1 Tmol H2	30 km	10,45	15,67	6,01	3,27	mWm^{-2}	-6,14	-4,96	-4,31	-3,53	mWm^{-2}	0,324	0,230	-0,146	0,300	mWm^{-2}
	38 km	18,42	24,16	16,85	11,10	mWm^{-2}	-7,71	-5,22	-5,49	-4,96	mWm^{-2}	-0,005	-0,064	0,003	0,229	mWm^{-2}
	Latitude	60-30° S	0-30° N	30-60° N	60-90° N		60-30° S	0-30° N	30-60° N	60-90° N		60-30° S	0-30° N	30-60° N	60-90° N	

***	**	*

Table 5: Sensitivities of three net radiative forcings (H_2O, O_3, CH_4) to emission of H_2O, NO_x and H_2 depending on altitude and latitude of emission. Asterisk refer to statistical significance (Table 3).

Table 5 shows an overview of radiative sensitivities normalized to perturbation per emitted mole. The error potential is labeled according to the t-test, that was calculated for atmospheric composition changes and the related probabilities are listed in Table 3. The H_2O net RF of NO_x emission scenarios is statistically not significant according to the t-test. Note that the normalization to perturbation per emitted mole has a different magnitude for NO_x emission scenarios (gigamole). In contrast to NO_x emission scenarios, the H_2O net RF for H_2O emission scenarios are all statistically significant. Note that H_2O emission scenarios would contribute by far the most to net radiative forcing without the normalization, followed by NO_x and H_2 emission scenarios, which is mainly due to the large ratio of H_2O to NO_x and H_2 in the exhaust. The normalized O_3 net RF is significant for all three types of emission. NO_x emission scenarios show by far the largest O_3 net RF values, followed by H_2 and H_2O emission scenarios (if the order of magnitude is kept in mind). Normalized CH_4 net RF is significant for most NO_x emission scenarios, however the magnitude is small compared to the normalized O_3 net RF for NO_x emission.

6. Discussion of atmospheric composition changes and radiative forcing

This section addresses the relation of emission, atmospheric composition changes and radiative forcing. A variety of publications exist where idealized atmospheric composition changes are used for sensitivity studies of the radiative effect: Lacis et al. (1990), Hansen et al. (1997), de F. Forster and Shine (1997), where Riese et al. (2012) is one of the most recent ones. However, our approach adds a level of complexity, since we did not calculate the RF of idealized atmospheric composition changes, but of modelled atmospheric composition changes due to idealized emission scenarios. Hence, it is important to discuss the process of emission, followed by atmospheric composition changes and the radiative forcing.

6.1. Water vapour atmospheric and radiative sensitivities

In the discussion of H_2O changes and their radiative forcing, we exclude NO_x emission scenarios, since they show no statistically significant results (see Table 4 and Table 5). Middle atmospheric H_2O perturbation for H_2O and H_2 emission

scenarios depends very much on altitude of emission and increases with altitude of emission. The H_2O perturbation lifetime follows more or less the Brewer-Dobson circulation, where H_2O emitted into the uprising tropical air has a larger lifetime than H_2O into the sinking polar air. In contrast to the increase with altitude, H_2O net RF develops a curvilinear trend and begins to decrease with mass perturbation (Fig. 31). The effect is small compared to the total perturbation. Two possible explanations

575 are, first, a saturation of reflected H_2O longwave radiation, and, second, altitude differences in peak H_2O mass accumulation with smaller radiative sensitivities for higher altitudes (Riese et al., 2012). In a prior publication (Pletzer et al., 2022), we did test H_2O net RF according to Myhre et al. (2009) and we deem a dependency of H_2O net RF to stratospheric H_2O background less likely. Fig. 34 shows vertical profiles of globally integrated H_2O concentration changes, which supports the second explanation in our opinion. To explain, excluding Southern Hemisphere scenarios, the peak accumulation is at higher altitudes

580 for scenarios where the trend of H_2O net RF deviates more from the linear trend in Fig. 31. Hence, an altitude and or latitude shift of the main mass accumulation to higher values should cause the lower H_2O net RF. Grewe et al. (2014a) and Wilcox et al. (2012) reported a nearly linear dependency of stratospheric adjusted RF to emission magnitude for a range of 9.5-11.5 km. Apparently, there the radiative sensitivity to different magnitudes does not show curvilinear tendencies. In contrast, the radiative sensitivity shows a curvilinear trend around the tropopause (Fig. 2b, van Manen and Grewe, 2019). To summarize

585 briefly, two trends of atmospheric composition changes and radiative forcing oppose each other. First, the increase in H_2O perturbation with altitude and, second, the decreasing radiative sensitivity depending on altitude and latitude. The first dominates the H_2O net RF and the second is a second order variation of the H_2O net RF.

6.2. Ozone atmospheric and radiative sensitivities

All scenarios show a total O_3 depletion, however, also increases in O_3 at specific altitudes (Fig. 6, Fig. 4, Fig. 24). Hence,

590 regions of O_3 depletion are partly equilibrated by regions of O_3 increase in terms of total depletion. Clearly, the perturbation sensitivity to emission is complex. The radiative sensitivity further increases the complexity. Close to the tropopause and the tropics the radiative effect per unit mass change is large (Fig. 1, Riese et al., 2012). In addition, several authors reported O_3 climate sensitivities, where an increase in O_3 either cools or warms near-surface air depending on domain (Fig 1, Lacis et al., 1990; Fig. 7, Hansen et al., 1997). This inversion point is slightly below 30 km, above which an increase in O_3 causes cooling

595 of near-surface air. Even though the emission altitudes in this publication are 30 and 38 km and hence above the inversion point, the regions of O_3 increase or decrease are very much distributed at different altitude and latitude regions, where each region has its specific radiative sensitivity. Therefore, the regions with O_3 changes combined with the active radiative sensitivity there form a complex net total of warming and cooling. Since the O_3 net RF is positive for all NO_x emission scenarios, we expect to see either O_3 depletion and hence warming at high altitudes and O_3 increase and hence warming at

600 lower altitudes.

For presentation of stratospheric trace gas changes volume mixing rations are often preferred, e.g. because they are unaffected by transport processes. However, radiation impacts are mainly affected by density changes and this might change the point of view. For example, perturbations close to the tropopause might appear low as mixing ratios, but are larger in numbers due to higher air densities compared to higher altitude mixing ratio changes. Fig. 35 gives a direct comparison of profiles of density and volume mixing ratio changes. Many NO_x emission scenarios (Fig. 35, mid) show an increase in O_3 density from 9 km (300 hPa) upwards, which switches to a decrease between around 16 and 25 km (100 and 25 hPa) depending on the specific emission scenario. To summarize, while the total density increase is smaller than the total density decrease, the region of increase comes with a significantly larger radiative sensitivity, which explains the radiative warming associated with reported total O_3 depletion in the scenarios. For H_2O and H_2 emission scenarios regions of O_3 depletion and O_3 increase in combination with radiative sensitivities cause cooling in contrast to NO_x emission scenarios. Here, the distribution of perturbations in combination with radiative sensitivities results in the opposite result to O_3 changes by NO_x emissions.

In summary, both the radiative sensitivity and the location of perturbation patterns along latitude and altitude are crucial for the interpretation of the results. The radiative sensitivity is generally largest at the tropics and close to the upper-troposphere lower-stratosphere, while the perturbation patterns are complex and differ depending on emitted trace gas.

7. General discussion

In the previous sections we concentrated on the main sensitivities of hypersonic emissions. Processes that are generally important, but with respect to the effect of hypersonic emissions are only of secondary importance, are discussed here. This comprises the discussion of polar stratospheric clouds and heterogeneous chemistry and the net production of H_2O from hypersonic aircraft emissions. We include a comparison to results from literature about atmospheric impacts of supersonic aircraft and synergy effects of simultaneous emissions.

7.1. Polar stratospheric clouds

Throughout this publication we focused on homogeneous, i.e. gas phase, atmospheric composition, since most of the emissions affect atmospheric regions outside (spatial and temporal) polar night and spring processes. The HS-sens model setup includes heterogeneous chemistry, i.e. particle effects like nucleation or condensation, which play a major role in polar stratospheric clouds, as well as chlorine and bromine activation of those particles. There are two reasons, why this is important for hypersonic aircraft emission. First, sedimentation of nitric acid trihydrate (NAT) and ice particles transport both, HNO_3 and H_2O, from high to lower altitudes (Iwasaka, Yasunobu and Hayashi, Masahiko, 1991; Crutzen and Arnold, 1986), which effectively increases denitrification and dehydration and in turn could reduce perturbation lifetimes. Clearly, the effect only contributes to the vertical transport, which is dominated by the residual circulation in the middle atmosphere. Second, the chemistry within

630   polar stratospheric clouds, where unreactive chlorine becomes reactive, heavily depletes O_3 concentrations and is prolonged by denitrification (Pyle, 2015, p.p. 248). In HS-sens model results, HNO_3 mixing ratios are increased between 100-10 hPa for NO_x emission scenarios. For H_2O and H_2 emission scenarios the mixing ratios are increased at around 10 hPa, depleted between 100-10 hPa and increased at and below 100 hPa (not shown). The effect is significant in most regions for the former and to a lesser extent for the latter. Sedimentation change of HNO_3 (excluding H_2 emission scenarios) and ice appears at 10-100 hPa,

635   with a peak between 10-20 hPa and is increased particularly in the lower polar stratosphere at approximately 200 hPa, but peaks not appear below the tropopause. According to Iwasaka, Yasunobu and Hayashi, Masahiko (1991) only NAT particles grown in the upper polar stratospheric clouds can reach the troposphere and ice particles are the ones that evaporate in the lower stratosphere. In the EMAC model the vertical falling distance is defined by the sedimentation velocity, which depends on the mean radius and a sedimentation factor (Kirner et al., 2011). Hence, the emitted trace gases, which become part of polar

640   stratospheric cloud chemistry and sedimentation, should not become large particles, since they do not reach the troposphere. In summary, polar stratospheric clouds affect atmospheric composition by an enhanced vertical transport, which in turn affects nitrogen oxide concentrations to a larger extent compared to H_2O concentrations. The effect becomes obviously more important for emission at high latitudes.

7.2. Net production of water vapour

645   Pletzer et al. (2022) showed that the emission of H_2O, H_2 and NO_x result in a net-production of H_2O, which overcompensates the H_2O depletion and increases the initial annual emission to some extent. In the study the origin of the effect, whether it comes from H_2O, H_2 or NO_x emission, was not clear. In the HS-sens simulation setup with independent emissions, we see that the overcompensation is largest for H_2O and H_2 emission scenarios and to a small extent appears in NO_x emission scenarios (not shown). The overcompensation is driven by oxidation in all scenarios and particularly an enhanced HNO_3 and CH_4

650   oxidation are very important. H_2 oxidation has a larger role in H_2 emission scenarios only.

7.3. Comparison to current literature on supersonic aircraft

The sensitivities to emissions of supersonic aircraft have recently been reviewed by Matthes et al. (2022). They describe the effect of NO_x on O_3 and state that an inversion point of emission exists at 17 km below which emission of NO_x increases total O_3 (Zhang et al., 2021b). Hypersonic aircraft cruising at 30 or 38 m show no clear picture and depletion of O_3 decreases or

655   increases depending on latitude of emission with altitude. The importance of H_2O emissions of supersonic aircraft and their effect on O_3 are highlighted, which we can further underline, since the total O_3 depletion due to H_2O emission is sometimes only a factor different to NO_x emission depending on scenario and the decreasing O_3 depletion with altitude for NO_x emission scenarios is compensated if combined with H_2O emission scenarios. Note that this depends very much on the ratio of emitted NO_x and H_2O and may easily change for a different ratio of exhaust. Matthes et al. (2022) further report that supersonic aircraft

660   affect the CH_4 lifetime through O_3 changes and increased OH availability and an increased UV radiation in the troposphere.

According to them the effect is comparably less important than the others. However, as shown in Pletzer et al. (2022), according to the trend calculated by both their models, CH_4 radiation changes might be more important for hypersonic aircraft compared to supersonic aircraft, where cooling by CH_4 changes compensates approximately a third of warming by O_3 changes (LMDZ-INCA model). In this study total CH_4 depletion for H_2O emission scenarios clearly increases with altitude and hence might the cooling associated with it, but open questions on the order of magnitude of radiative forcing by CH_4 changes remain.

7.4. Synergy effects of simultaneous emissions

In the HS-sens model setup we look at each emission independently. For comparison, Kinnison et al. (2020) calculated single (H_2O, NO_x) and simultaneous emission, which we decided against for two reasons. First, due to their results - we have the impression that their single emission perturbations add up to the simultaneous emission perturbation (Fig. 6-8, Kinnison et al., 2020) - and, second, to avoid a substantial increase in computation time. The results of this publication (e.g. Fig. 31) are very similar in magnitude compared to the combined emission calculated in Pletzer et al. (2022). Hence, effects due to simultaneous emission should at most be second order effects with small impact in comparison to the total effect.

7.5. Comparison to land hydrogen emissions

Ocko and Hamburg (2022) combined multiple studies and made a comparison of (indirect) radiative efficiencies or in our words radiative sensitivities to H_2 emission with other land emissions. Here, 'indirect' refers to tropospheric CH_4 and O_3 changes and stratospheric H_2O changes due to H_2 emissions. Recalculated, their sensitivities to land H_2 emission amount to 0.7-1.0 $mW(m^2 \cdot TmolH_2)^{-1}$, which include the stratospheric effects. In this comparison the combined, i.e. from ozone and water vapour, average radiative sensitivity (approx. 8.0 $mW(m^2 \cdot TmolH_2)^{-1}$) to hypersonic aircraft H_2 emissions (Table 5), is up to one order of magnitude larger than the radiative sensitivity to land H_2 emission.

8. Summary

In this study we analyzed sensitivities with respect to location and emission type of hypersonic emissions, and showed, first, how emissions of hypersonic aircraft (H_2O, NO_x, H_2) affect atmospheric composition and, second, how this change in atmospheric composition affects climate, i.e. stratospheric-adjusted radiative forcing. The novelty here is the systematic emission at two different altitude regions (30 km, 38 km) and four different latitude regions (60-30° S, 0-30° N, 30-60° N, 60-90° N) and the individual impact of NO_x, H_2O and H_2 emissions.

Atmospheric perturbations were calculated with the full-scale atmospheric chemistry and general circulation model EMAC and the perturbations were fed to a radiation model to calculate the stratospheric-adjusted radiative forcing. Additionally, the study includes an evaluation of EMAC H_2O and O_3 mixing ratios. Briefly summarized, the model excels in modelling O_3 and

underestimates H_2O mixing ratios in the middle atmosphere. The model setup was based on a novel approach to reduce the
690   cost of computation and effectively reduced the simulated years by one-third.

The method to calculate changes in atmospheric composition and associated stratospheric-adjusted radiative forcings for different emission regions allows a comparison of their specific sensitivities. The main results are condensed in two quick-look tables of atmospheric and radiative sensitivities (Table 4, Table 5), visualized in Fig. 10, and other results are mostly for explanation and analysis. The main message is that sensitivities can differ manifold depending on latitude and altitude of
695   emission. The most important large-scale process controlling the lifetime of perturbations certainly is the Brewer-Dobson circulation. But also local processes like polar stratospheric cloud chemistry can contribute strongly depending on emission location. From the calculated sensitivities H_2O emission and the related H_2O perturbation in addition to NO_x emission which causes O_3 perturbation have the largest warming potential. Both share the regional pattern (except NO_x emission at 38 km), that emission at low latitudes is associated with the largest radiative sensitivities. However, their altitude sensitivities are
700   (mostly) inverse, i.e. warming from H_2O perturbation increases with altitude, while warming from O_3 changes decreases with altitude at 30-38 km. It might appear in Fig. 10 that regions of largest water vapour changes in mid-latitudes and polar regions do not overlap very much with the regions of largest radiative sensitivities in the tropics. However, the overlap clearly suffices to cause significant values of stratospheric-adjusted radiative forcing. The calculated sensitivities allow inexpensive and fast estimates of the stratospheric-adjusted radiative forcing of new hypersonic aircraft designs depending on latitude, altitude and
705   ratio of emissions without the need to apply a complex atmospheric chemistry general circulation model.
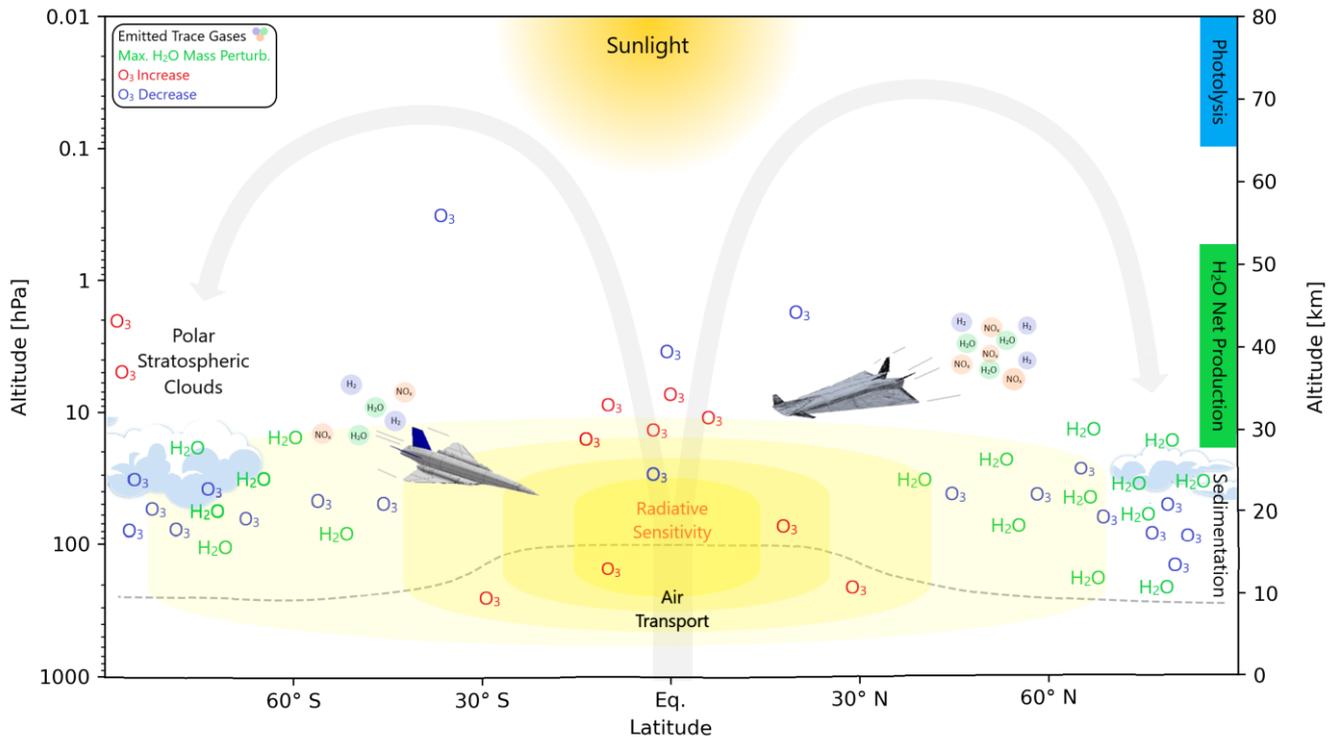
Figure 10: Overview of the average atmospheric sensitivities of water vapour and ozone to hypersonic emissions of water vapour, nitrogen oxides and hydrogen and the most important atmospheric processes. Show in yellow is the approximate radiative sensitivity to trace gas changes.

710 Generally, the results are in line with prior publications (Kinnison et al., 2020; Pletzer et al., 2022) and the altitude optimization potential has already been highlighted by Kinnison et al. (2020) for atmospheric composition changes and Pletzer et al. (2022) for atmospheric composition changes and radiation. An additional highlight is an extension of the H_2O perturbation lifetime in literature to higher levels (Fig. 8). Further work may include the analysis of HS-sens model results with respect to the seasonal sensitivity that may enhance the mitigation potential when adapting aircraft trajectories to the seasonal changes in

715 circulation and chemistry.

9. Code availability

The Modular Earth Submodel System (MESSy) is continuously further developed and applied by a consortium of institutions. The usage of MESSy and access to the source code is licensed to all affiliates of institutions that are members of the MESSy Consortium. Institutions can become a member of the MESSy Consortium by signing the MESSy Memorandum of

720 Understanding. More information can be found on the MESSy Consortium Website (http://www.messy-interface.org, last

access: 14 July 2023). The submodel H2OEMIS used here has been implemented in MESSy version 2.54.0 and is available in the current devel branch

10. Data availability

For access to datasets of EMAC results please contact Johannes Pletzer.

725 **11. Appendices**

11.1. Methods and simulations

11.1.1. EMAC model setup HS-sens

In the HS-sens model setup we used the following submodels for physics: AEROPT (Aerosol OPTical properties), CLOUD, CLOUDOPT (CLOUD OPTical properties), CONVECT (CONVECTion), CVTRANS (ConVective Tracer TRANSport),
730 E5VDIFF (ECHAM5 Vertical DIFFusion), GWAVE (Gravity WAVE), OROGW (OROgraphic Gravity Wave), QBO (Quasi Biannual Oscillation) and RAD (RADiation).

AEROPT calculates aerosol optical properties and CLOUDOPT cloud optical properties (Dietmüller et al., 2016). CLOUD accounts for cloud cover, cloud micro-physics and precipitation and is based on the original ECHAM5 subroutines, as is CONVECT, which calculates convection processes (Roeckner et al., 2006). CVTRANS is directly linked and calculates the
735 transport of tracers due to convection. E5VDIFF addresses vertical diffusion and land-atmosphere exchanges excluding tracers. GWAVE and OROGW account for (non-)orographic gravity waves. QBO includes winds of observed quasi-biannual-oscillations. RAD and RAD_FUBRAD contain the extended ECHAM5 radiation scheme and allow multiple radiation calls like stratospheric adjusted radiative forcing (Dietmüller et al., 2016).

For chemistry, we used the following submodels: AIRSEA, CH4, DDEP (Dry DEPosition), H2OEMIS (H2O EMISsion),
740 JVAL (J Values), LNOX (Lightning Nitrogen OXides), MECCA (Module Efficiently Calculating the Chemistry of the Atmosphere), MSBM (Multiphase Stratospheric Box Model), OFFEMIS (OFFline EMISsion), ONEMIS (ONline EMISsion), SCAV (SCAVenging), SEDI (SEDImentation), SURFACE and TNUDGE (Tracer NUDG(E)ing) and TREXP (Tracer Release EXPeriments).

AIRSEA calculates the deposition and emission over the ocean, which corrects the global budget of tracers like methanol and
745 acetone (Pozzer et al., 2006). CH4 determines the oxidation of methane (CH_4) by the hydroxyl radical OH, atomic oxygen $O(^1D)$, chlorine and photolysis (Winterstein and Jöckel, 2021). In the HS-sens setup the feedback to specific humidity is activated in MECCA. DDEP accounts for the dry deposition of aerosol tracers and gas phase tracers and SEDI for the

sedimentation of aerosols and their components (Kerkweg et al., 2006). H2OEMIS adds H_2O emissions to specific humidity via TENDENCY (Pletzer et al., 2022). JVAL calculates the photolysis rate coefficients (Sander et al., 2014). LNOX contributes a parametrization (Grewe) for NO_x production by lightning for intra-clouds and clouds-to-ground (Grewe et al., 2001; Tost et al., 2007). MECCA accounts for all internal tracers related to production and destruction of chemical components (Sander et al., 2005; Sander et al., 2011). MSBM calculates the polar stratospheric cloud-chemistry and is based on the PSC (Polar Stratospheric Cloud) submodel code (Jöckel et al., 2010). The representation of polar stratospheric clouds includes three subtypes of polar stratospheric clouds, i.e. solid nitric acid trihydrate (NAT) particles (type 1a), super-cooled ternary solutions (HNO_3, H_2SO_4, H_2O, type 1b) and solid ice particles (type 2) (Kirner et al., 2011). The latter start to form below the frost point. Multiple parameters regarding polar stratospheric clouds are written as output within EMAC. Examples are mixing ratios of relevant trace gases (HNO_3, HCl, HBr, HOCl, HOBr) in liquid, solid or gas phase, number densities of ice and NAT particles and loss and production of NAT through sedimentation. Further included are the physical parameters velocity and radius and surface of particles. OFFEMIS prescribes emission data like relative concentration pathways (RCPs) and ONEMIS calculates emissions online; both are added to internal tracer tendencies (Kerkweg et al., 2006). SCAV accounts for wet deposition and liquid phase chemistry in precipitation fluxes (Tost et al., 2006). SURFACE originates from several ECHAM5 subroutines and calculates temperatures of different surfaces (Roeckner et al., 2006). TNUDGE is responsible for tracer nudging (Kerkweg et al., 2006).

Additional diagnostics were activated via the following submodels: CONTRAIL, DRADON (Decay RADioactive ONline), O3ORIG (O3 ORIGin), ORBIT, PTRAC (Passive TRACer), SATSIMS (Satellites Simulator), SCALC (Simple CALCulations), TBUDGET (Tracer BUDGET), TENDENCY, S4D (Sampling in 4 Dimensions), SCOUT (Stationary Column OUTput), SORBIT (Satellite ORBIT), TROPOP (TROPOsPhere) and VISO (Vertically layered ISO-surfaces and maps). We mainly used PTRAC for verification of emitted trace gases, TENDENCY to account for and verify the specific humidity budget and TROPOP for the global WMO tropopause height during post-analysis.

770   **11.1.2. Evaluation with satellite data**
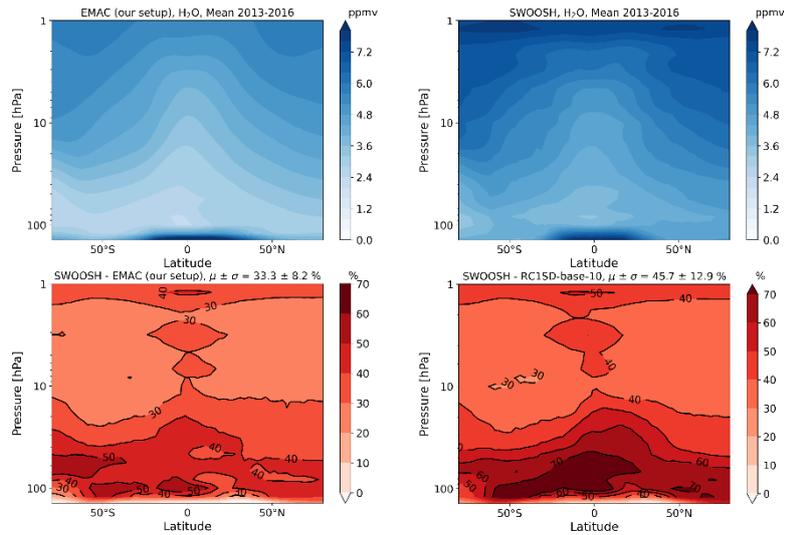
Figure 11: Multi-annual mean of water vapour volume mixing ratio for the EMAC setup, used in this work (upper left), SWOOSH multi-instrumental mean satellite data (upper right) and the difference (observation-model) in percent for our model setup (lower left) and RC1SD-base-10 (lower right).

775
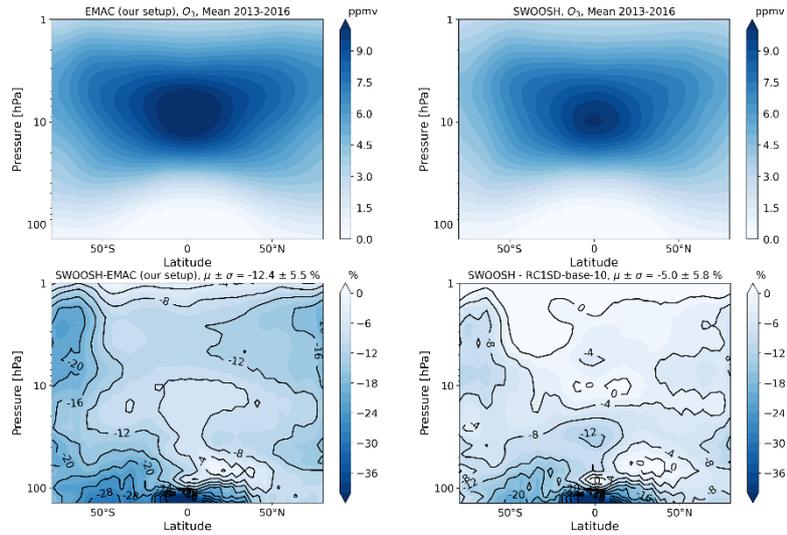
Figure 12: Multi-annual mean of ozone volume mixing ratio for the EMAC setup, used in this work (upper left), SWOOSH multi-instrumental mean satellite data (upper right) and the difference (observation-model) in percent for our model setup (lower left) and RC1SD-base-10 (lower right).

11.1.3. Enhancing the efficient use of computing resources
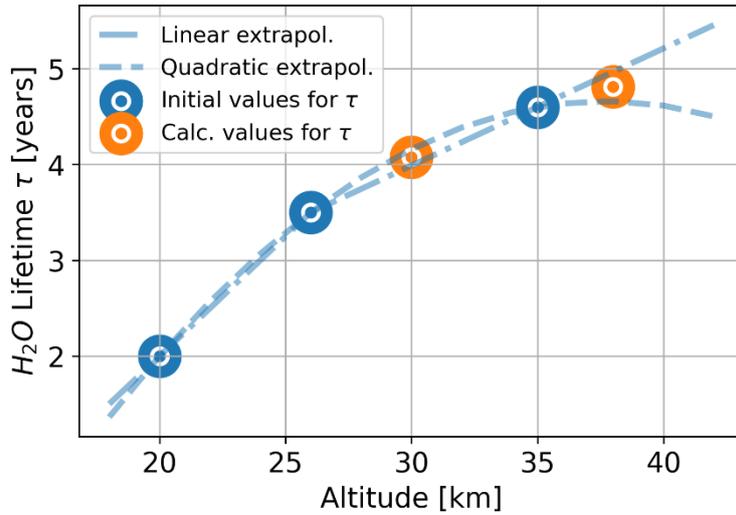
Figure 13: Water vapour perturbation lifetime τ depending on altitude. Blue circles represent initial data, that were used for inter- and extrapolation of orange data circles. Dashed and dashed-dotted blue lines show the behavior of quadratic and linear inter- and extrapolation, respectively. Orange data circles are based on the average of linear and quadratic inter- and extrapolation. The values of the orange circles were used to calculate s with Eq. (6).

11.2. Emission scenarios

11.2.1. Timeline and validation
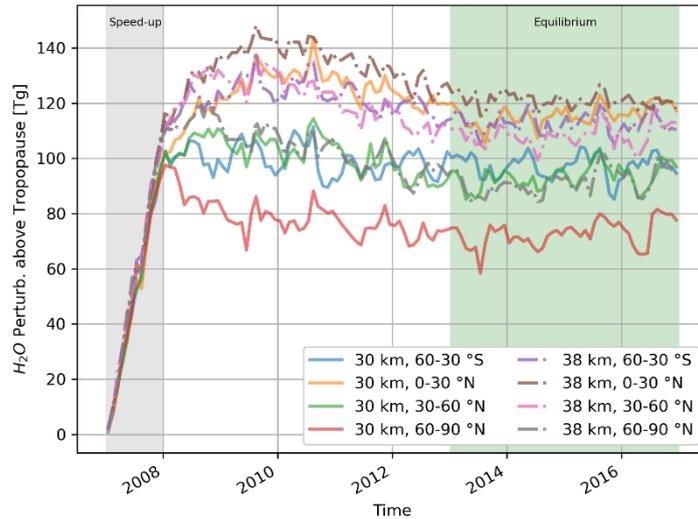
Figure 14: Timeline of monthly mean water vapour perturbation in teragram for scenarios, where water vapour is emitted. The first year (gray shaded area) shows the enhanced emission by the factor s, i.e. the speed-up. 2013-2016

 (green shaded area) shows the years in multi-annual mean equilibrium. The white and gray shaded area (2007-2012) marks the spin-up phase.

11.3. Atmospheric composition changes

11.3.1. Methane lifetime
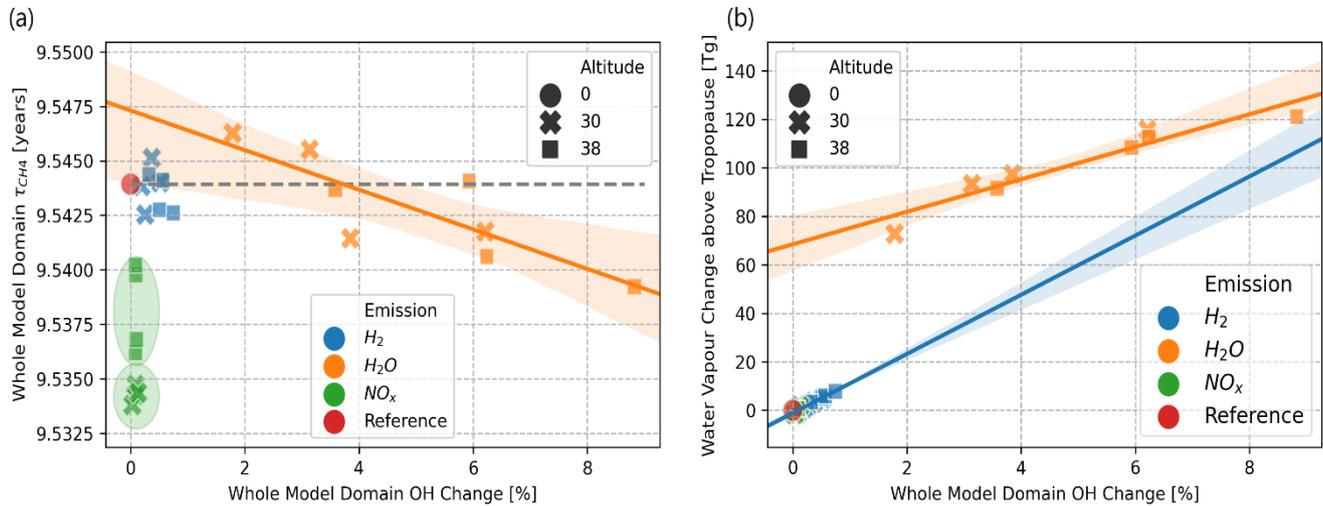
795 **Figure 15: Methane lifetime (whole model domain) is shown in (a) and the water vapour mass perturbation (b) in relation to the relative hydroxyl radical mass change (whole model domain) for all emission scenarios (legend). Whole model domain methane lifetime is reduced or extended below or above the dashed gray line, respectively. The regression lines including the shaded areas depict the mean and standard deviation of scenarios.**
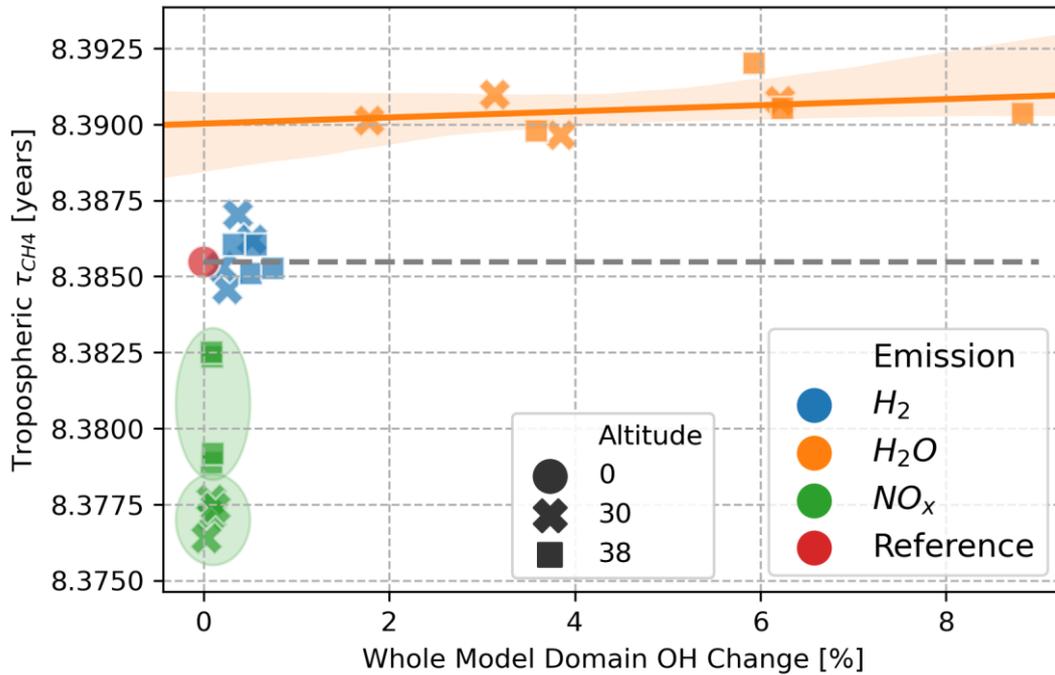
 Figure 16: Tropospheric methane lifetime in relation to hydroxyl change (whole model domain) for all emission scenarios (legend). Tropospheric methane lifetime is reduced or extended below or above the dashed gray line, respectively. The regression lines including the shaded areas depict the standard deviation of scenarios.

11.3.2. Water vapour emission
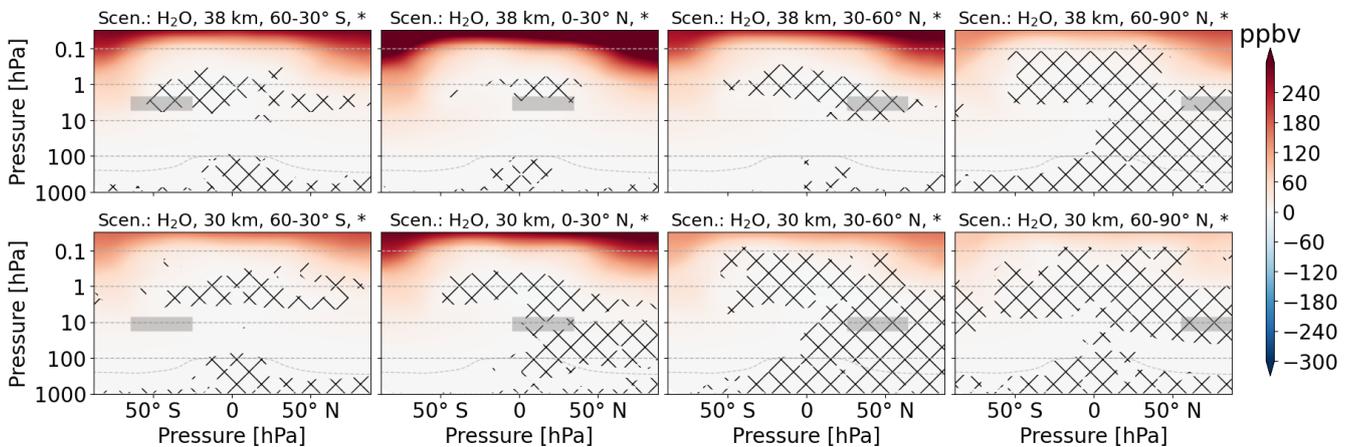
805 **Figure 17: Zonal mean of H_2 perturbation (volume mixing ratio, ppbv) for scenarios where H_2O is emitted. The first and second row refer to 38 km and 30 km altitude of emission, respectively. Columns represent the latitude region of emission. The emission regions are shaded in gray. Lines indicate statistical insignificant results and the probability level is written in the title of each subplot.**
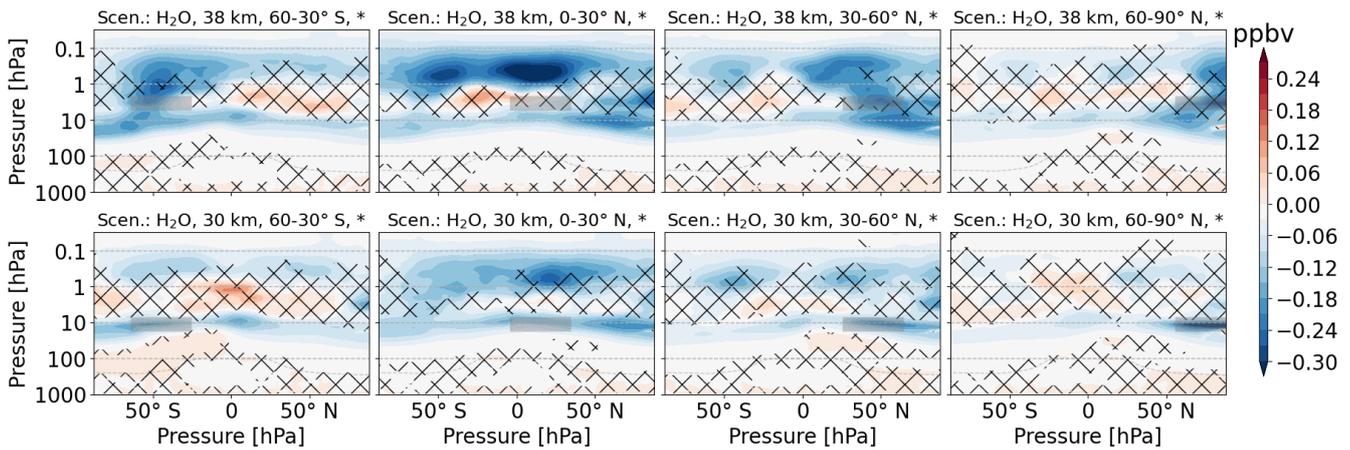
Figure 18: Zonal mean of NOₓ perturbation (volume mixing ratio, ppbv) for scenarios where H₂O is emitted. The first and second row refer to 38 km and 30 km altitude of emission, respectively. Columns represent the latitude region of emission. The emission regions are shaded in gray. Lines indicate statistical insignificant results and the probability level is written in the title of each subplot.

11.3.3. Nitrogen oxide emission and ozone perturbation
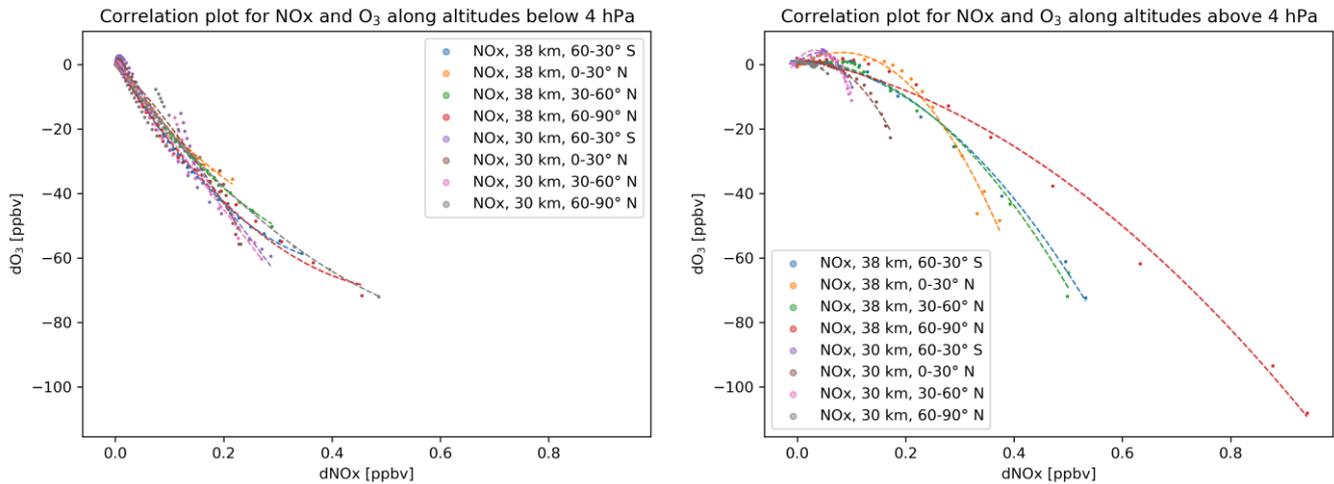
Figure 19: Correlation of nitrogen oxide change and ozone change for two altitudes regions (surface-4 hPa and 4-0.01 hPa). The values are averaged over latitude and limited to statistically significant values with a 95 % confidence.
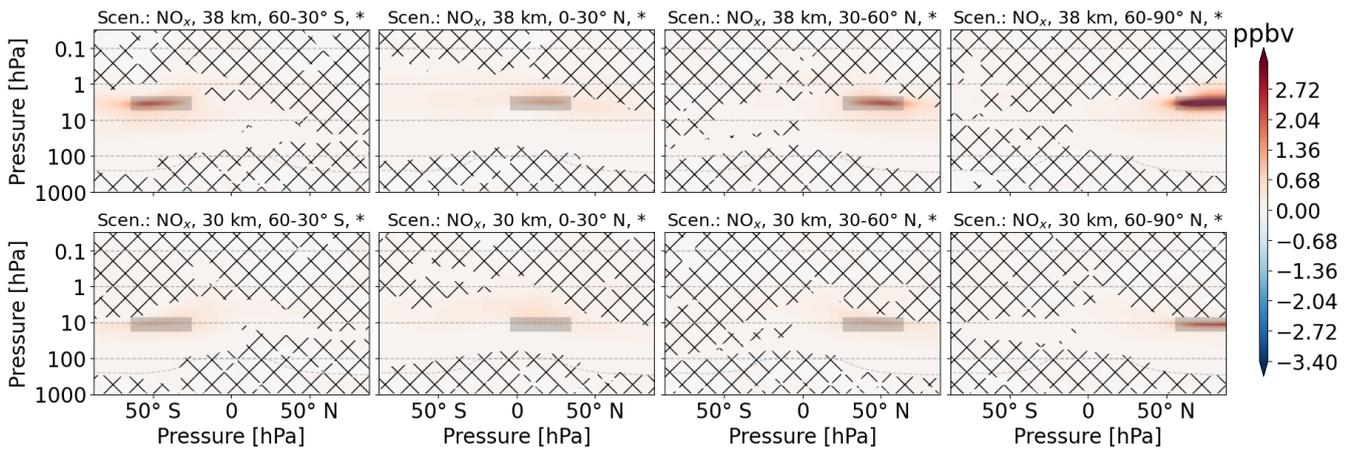
Figure 20: Zonal mean of NOₓ perturbation (volume mixing ratio, ppbv) for scenarios where NOₓ is emitted. The first and second row refer to 38 km and 30 km altitude of emission, respectively. Columns represent the latitude region of emission. The emission regions are shaded in grey. Lines indicate statistical insignificant results and the probability level is written in the title of each subplot.
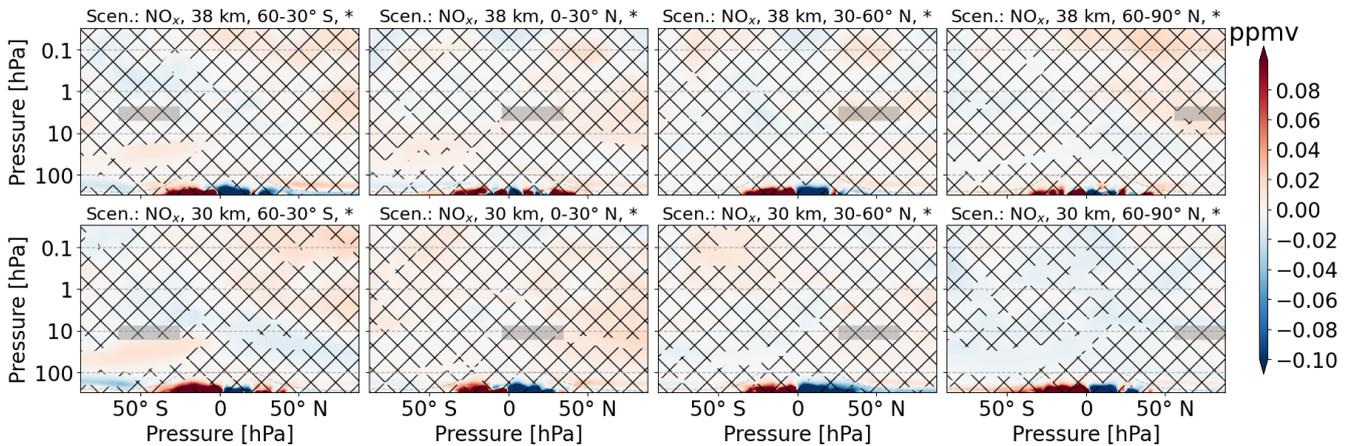
Figure 21: Zonal mean of H₂O perturbation (volume mixing ratio, ppbv) for scenarios where NOₓ is emitted. The first and second row refer to 38 km and 30 km altitude of emission, respectively. Columns represent the latitude region of emission. The emission regions are shaded in gray. Lines indicate statistical insignificant results and the probability level is written in the title of each subplot.
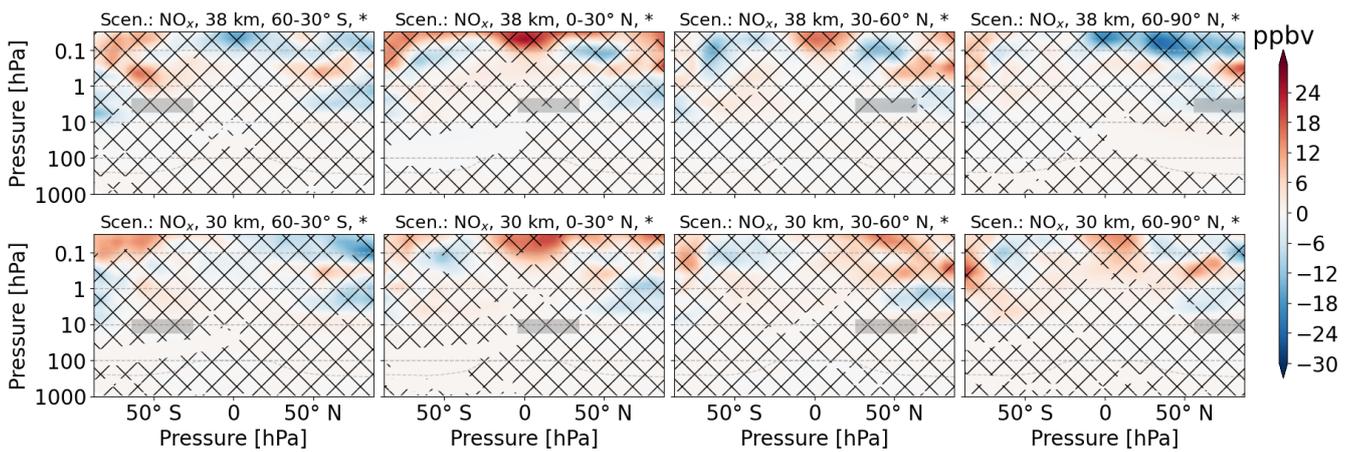
Figure 22: Zonal mean of H₂ perturbation (volume mixing ratio, ppbv) for scenarios where NOₓ is emitted. The first and second row refer to 38 km and 30 km altitude of emission, respectively. Columns represent the latitude region of emission. The emission regions are shaded in gray. Lines indicate statistical insignificant results and the probability level is written in the title of each subplot.
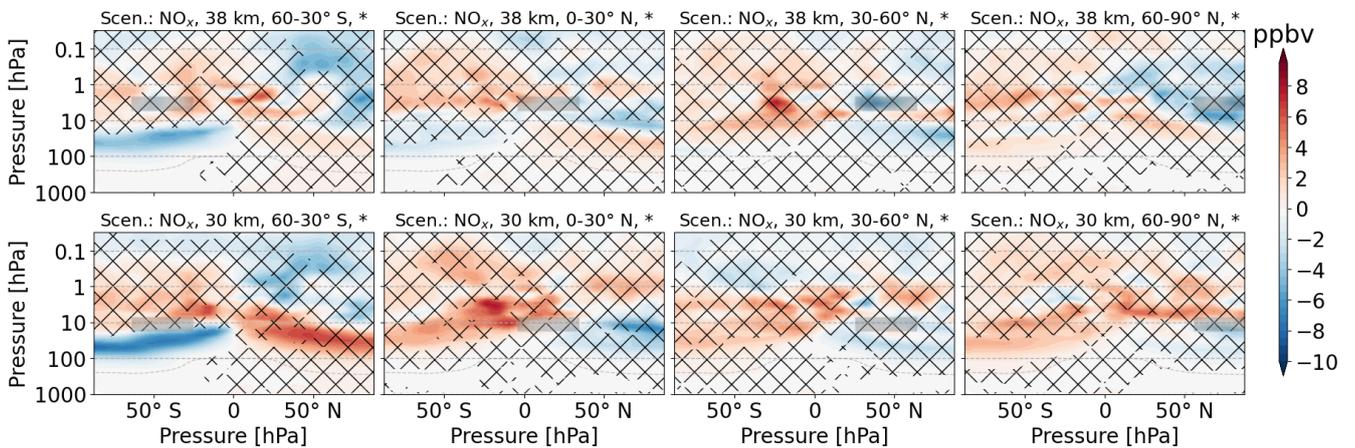
Figure 23: Zonal mean of CH₄ perturbation (volume mixing ratio, ppbv) for scenarios where NOₓ is emitted. The first and second row refer to 38 km and 30 km altitude of emission, respectively. Columns represent the latitude region of emission. The emission regions are shaded in gray. Lines indicate statistical insignificant results and the probability level is written in the title of each subplot.

11.3.4. Hydrogen emission
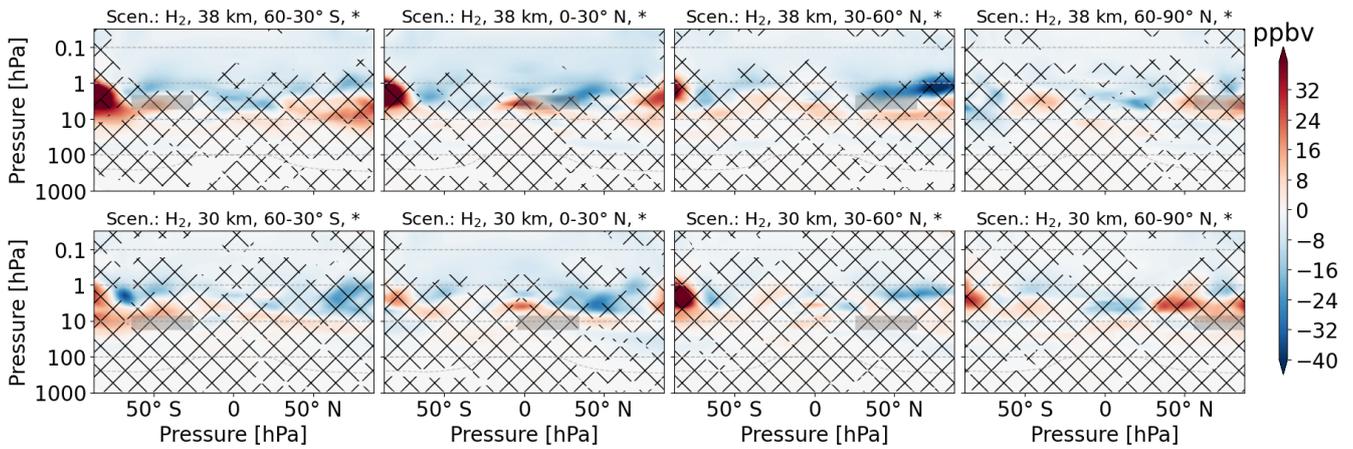
Figure 24: Zonal mean of O₃ perturbation (volume mixing ratio, ppbv) for scenarios where H₂ is emitted. The first and second row refer to 38 km and 30 km altitude of emission, respectively. Columns represent the latitude region of emission. The emission regions are shaded in gray. Lines indicate statistical insignificant results and the probability level is written in the title of each subplot.
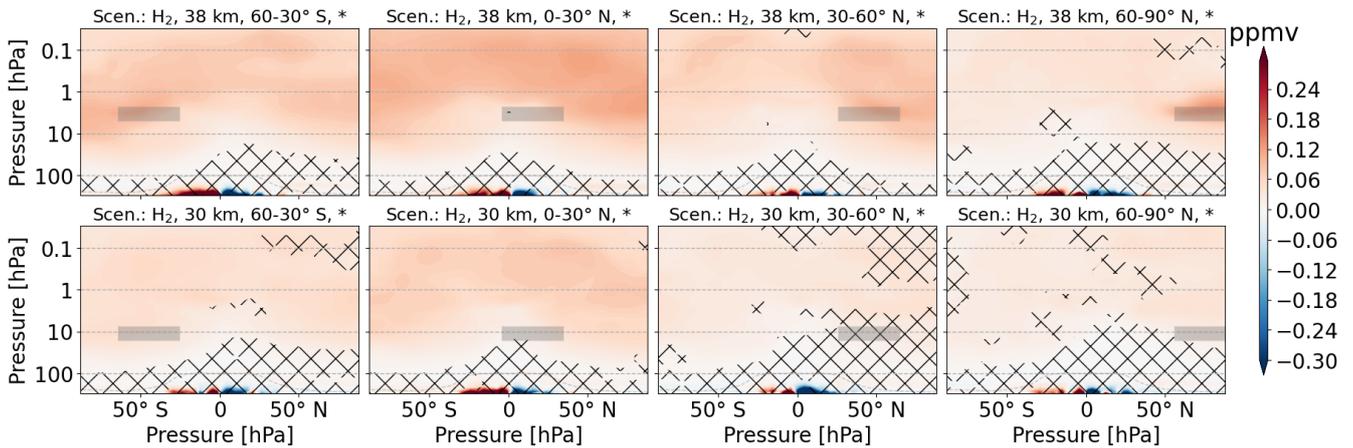
Figure 25: Zonal mean of H₂O perturbation (volume mixing ratio, ppmv) for scenarios where H₂ is emitted. The first and second row refer to 38 km and 30 km altitude of emission, respectively. Columns represent the latitude region of emission. The emission regions are shaded in gray. Lines indicate statistical insignificant results and the probability level is written in the title of each subplot.
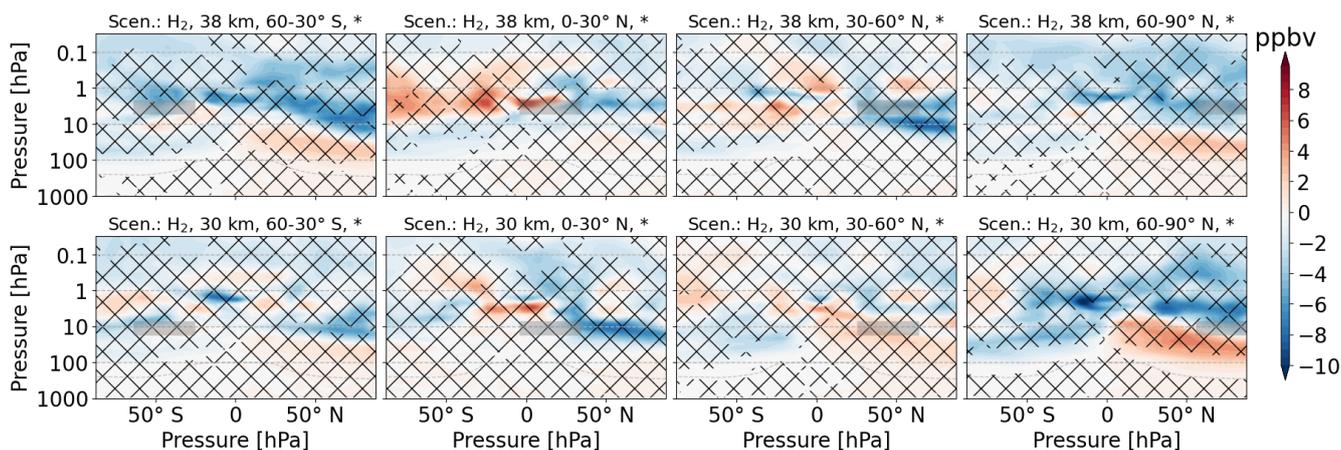
850 Figure 26: Zonal mean of CH_4 perturbation (volume mixing ratio, ppbv) for scenarios where H_2 is emitted. The first and second row refer to 38 km and 30 km altitude of emission, respectively. Columns represent the latitude region of emission. The emission regions are shaded in gray. Lines indicate statistical insignificant results and the probability level is written in the title of each subplot.
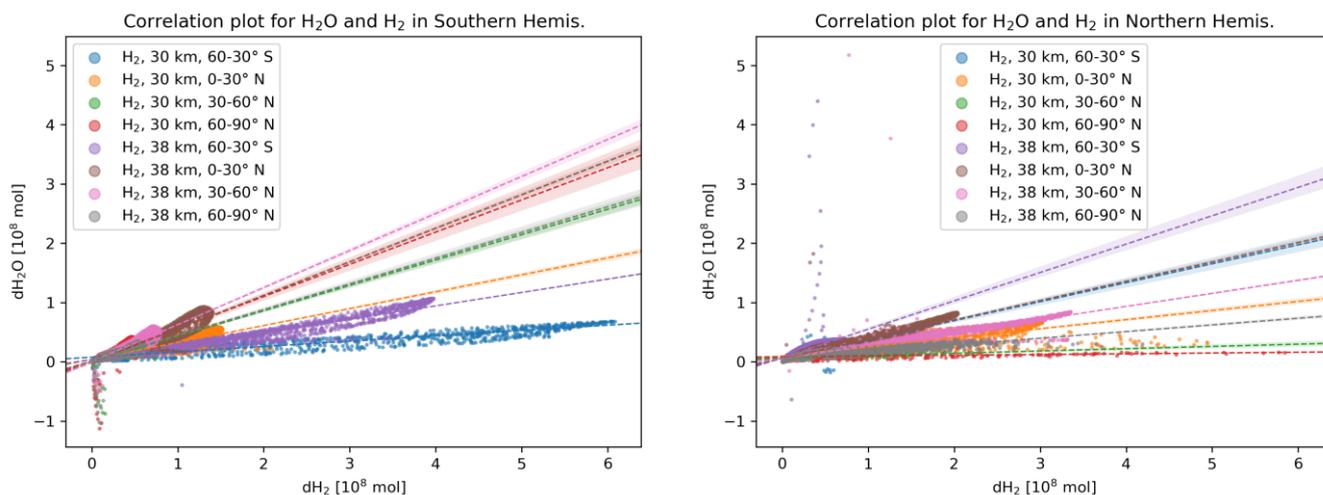
855 Figure 27: Correlation of molar water vapour and hydrogen change for the Southern (left) and Northern (right) Hemisphere. The values are limited to statistically significant values with a 95 % confidence.

11.3.5. Overview on atmospheric composition

Table 6: Average atmospheric composition changes per molecule of emitted species

Emission	ΔH_2O	ΔH_2O / molecule	ΔO_3	ΔO_3/ molecule
H_2O	~ 100 Tg	85 Tg (Tmol/year)$^{-1}$	-0.04 %	-0.03 % (Tmol/year)$^{-1}$
NO_x	~ 0 Tg	0 Tg (Tmol/year)$^{-1}$	-0.15 %	-242 % (Tmol/year)$^{-1}$
H_2	~ 5 Tg	42 Tg (Tmol/year)$^{-1}$	-0.02 %	-0.17 % (Tmol/year)$^{-1}$

Emission	Sphere	ΔCH4 [%]	ΔHO2 [%]	ΔOH [%]	ΔCH4/Tmol [%]	ΔHO2/Tmol [%]	ΔOH/Tmol [%]
H_2O	Troposphere	-0,0014	-1,12	-0,15	-0,001	-0,9	-0,1
H_2O	Middle Atmosphere	-0,0851	4,31	5,31	-0,072	3,7	4,5
NOx	Troposphere	-0,0015	0,05	0,07	-2,218	71,0	107,2
NOx	Middle Atmosphere	-0,0057	-0,44	0,09	-8,456	-655,1	126,6
H_2	Troposphere	-0,0002	0,02	-0,02	-0,002	0,1	-0,2
H_2	Middle Atmosphere	-0,0140	0,39	0,47	-0,120	3,3	4,0

860 **Table 7: Relative atmospheric composition change of CH₄, HO₂ and OH (average) for the troposphere and middle atmosphere**

11.4. Radiative forcing

11.4.1. Water vapour radiative forcing
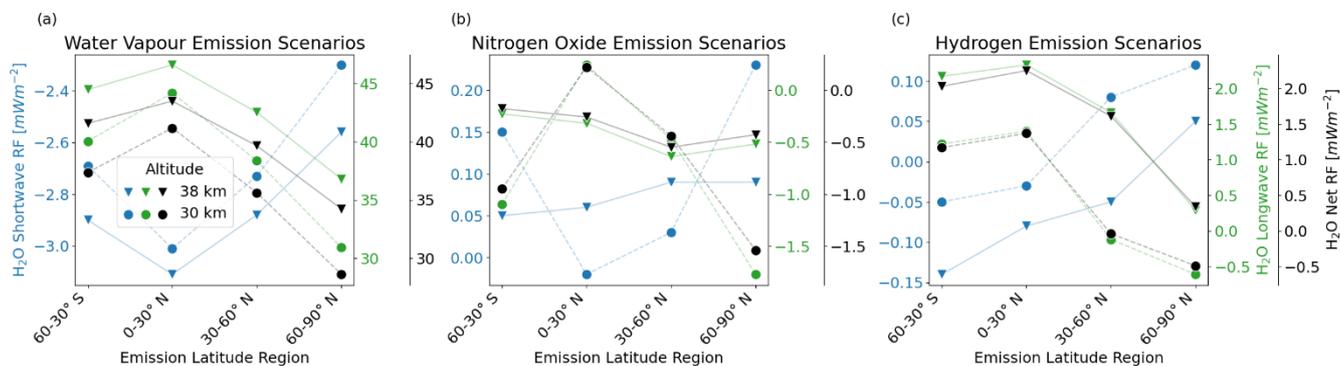
865 **Figure 28: The shortwave, longwave and net radiative forcing in blue, green and black, respectively, for water vapour (a), nitrogen oxide (b) and hydrogen (c) emission scenarios due to water vapour changes. For different altitude emission scenarios refer to markers. Latitude regions of emission are aligned on the x-axis.**

11.4.2. Ozone radiative forcing
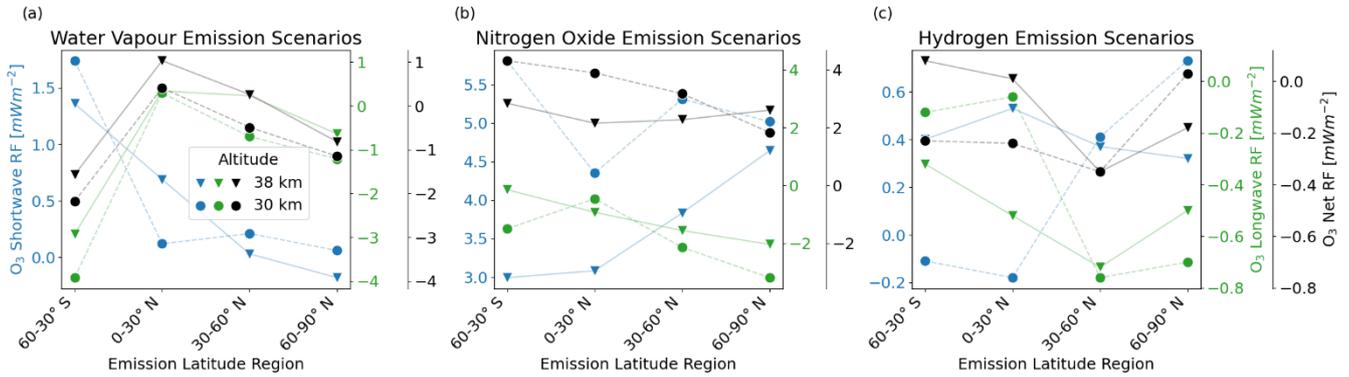
870 **Figure 29: The shortwave, longwave and net radiative forcing in blue, green and black, respectively, for water vapour (a), nitrogen oxide (b) and hydrogen (c) emission scenarios due to ozone changes. For different altitude emission scenarios refer to markers. Latitude regions of emission are aligned on the x-axis.**

11.4.3. Methane radiative forcing
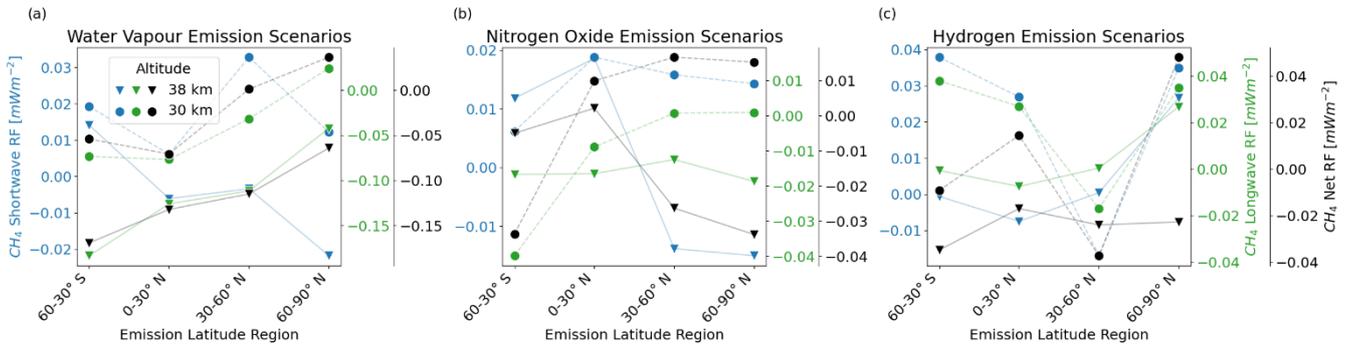
875 **Figure 30: The shortwave, longwave and net radiative forcing in blue, green and black, respectively, for water vapour (a), nitrogen oxide (b) and hydrogen (c) emission scenarios due to methane changes. For different altitude emission scenarios refer to markers. Latitude regions of emission are aligned on the x-axis.**

11.4.4. Individual radiative forcing and the related perturbations
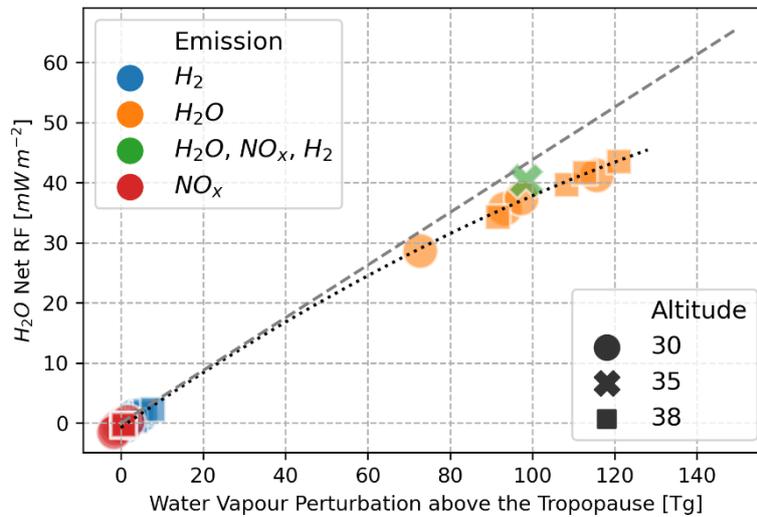
Figure 31: Overview of H₂O net radiative forcing for all 24 simulations. Colours refer to the initial emission (H₂, H₂O and NOₓ) and markers to altitude of emission. The green cross for 35 km altitude refers to the publication of Pletzer et al. (2022) and is based on a global emission scenario (aircraft LAPCAT MR2) where H₂, H₂O and NOₓ are emitted simultaneously. The gray line refers to a correlation of RF and H₂O perturbation from another publication (Fig. 8, Grewe et al., 2014a). The dotted black line is a two-dimensional polynomial fit with $ax^2 + bx + c$, where a = -0.88, b = 473.73 and c = -746.76 $Wm^{-2}Tg^{-1}$.
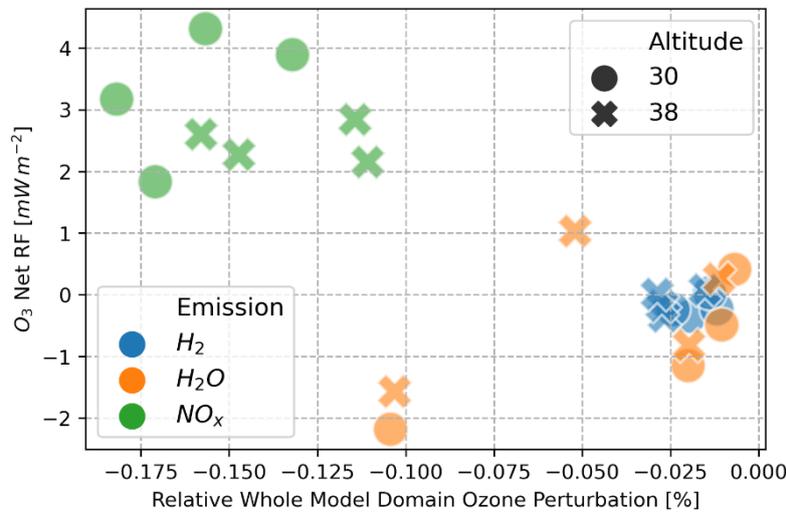
Figure 32: Overview of O₃ net radiative forcing for all 24 simulations. Colors refer to the initial emission (H₂, H₂O and NOₓ) and markers to altitude of emission.
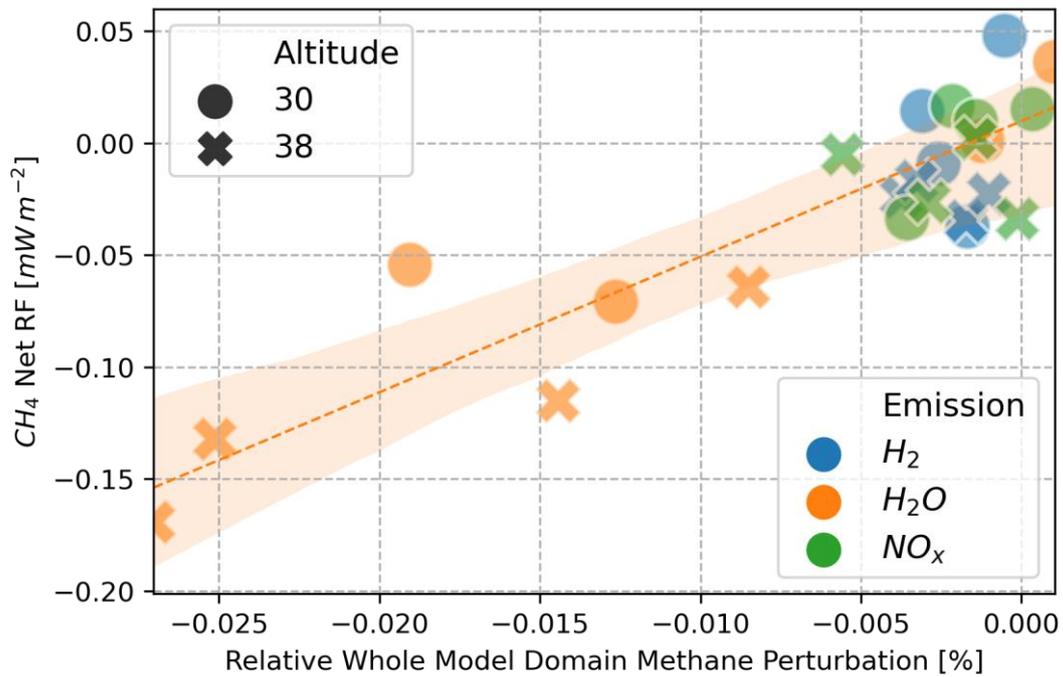
 Figure 33: Overview of CH₄ net radiative forcing for all 24 simulations. Colors refer to the initial emission (H₂, H₂O and NOₓ) and markers to altitude of emission. The regression line including the shaded areas depict the mean and standard deviation of the eight H₂O emission scenarios.

11.5. Discussion of atmospheric composition changes and radiative forcing

11.5.1. Water vapour atmospheric and radiative sensitivities
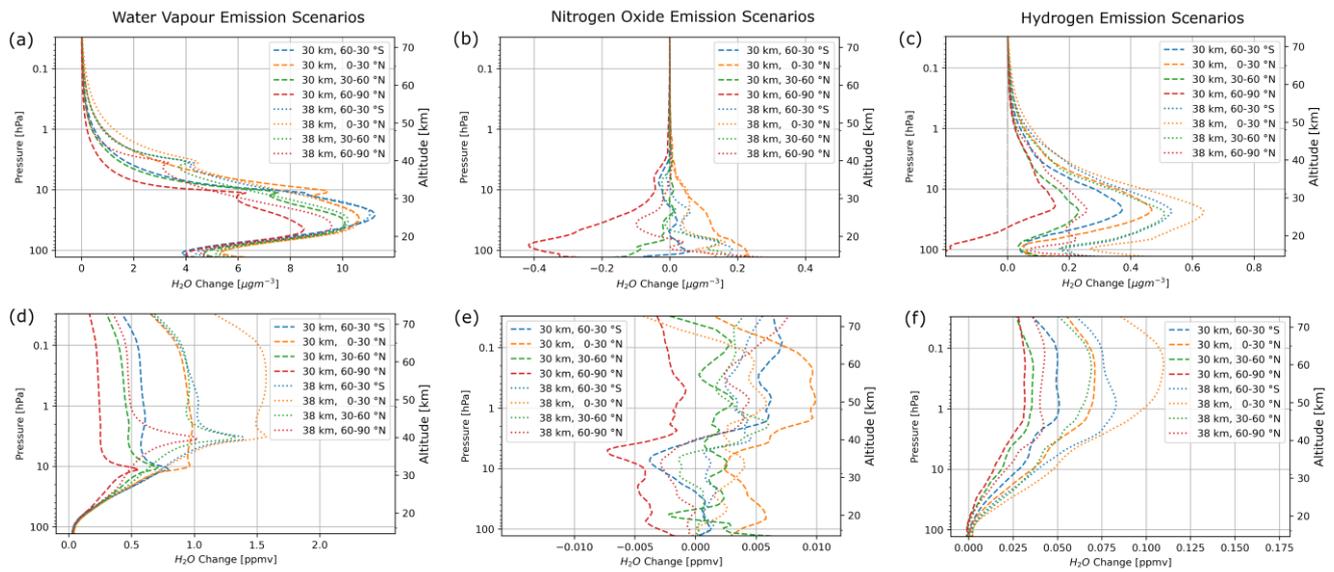
Figure 34: Vertical distribution of global H₂O change as concentration (a, b, c) and volume mixing ratio (d, e, f). Subfigures (a, d), (b, e) and (c, f) depict H₂O change due to H₂O, NOₓ and H₂ emission respectively,

11.5.2. Ozone atmospheric and radiative sensitivities
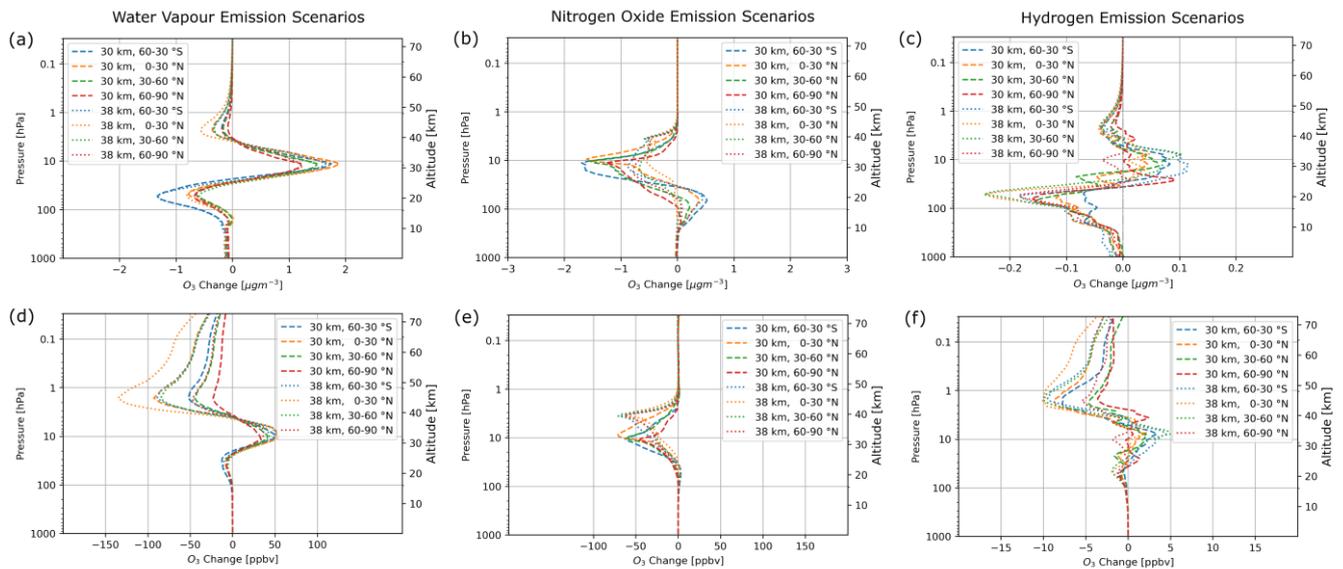
900 **Figure 35: Vertical distribution of global O_3 change as concentration (a, b, c) and volume mixing ratio (d, e, f). Subfigures (a, d), (b, e) and (c, f) depict O_3 change due to H_2O, NO_x and H_2 emission respectively,**

11.6. Conclusion and discussion
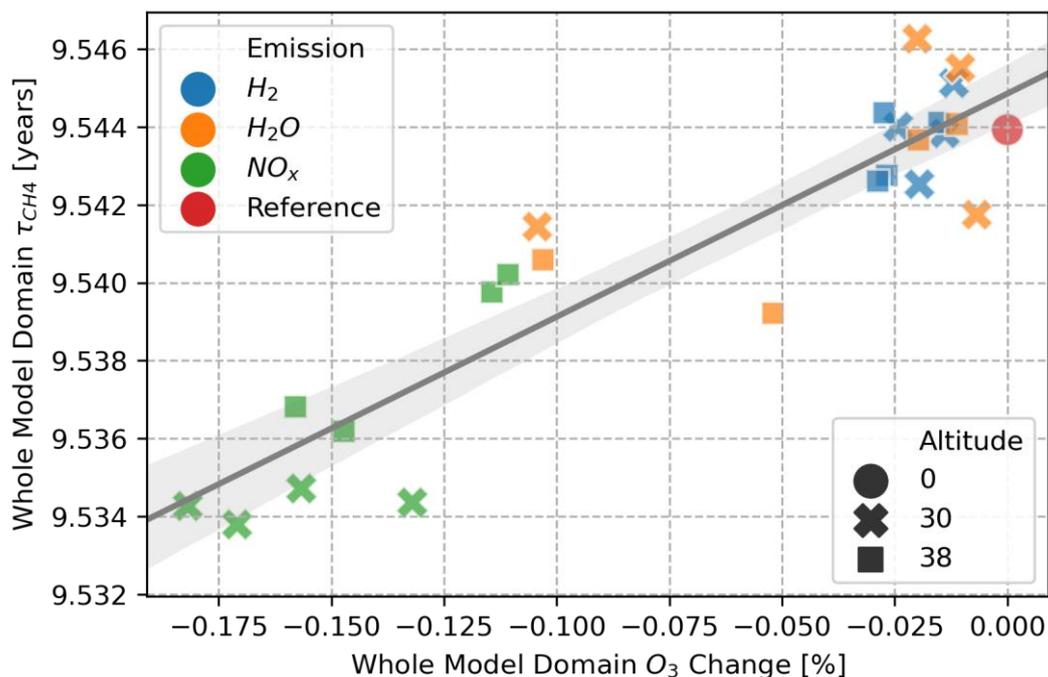
Figure 36: Methane lifetime in relation to ozone change (both whole model domain) for all emission scenarios (legend). The gray regression line including the shaded area depict the 95 % confidence interval of all scenarios.

12. Author contribution

Johannes Pletzer set up the EMAC model simulations, analyzed and post-processed the EMAC model results. Volker Grewe was involved in the discussion of the results and supported the writing of the document. The manuscript was written by Johannes Pletzer, then reviewed by the authors and approved by all the authors.

13. Competing interests

The authors declare that they have no competing interests.

14. Acknowledgements

The model simulations have been performed at the German Climate Computing Centre (DKRZ). The resources for the simulations were offered by the Bundesministerium für Bildung und Forschung (BMBF). We both thank kindly for this opportunity.

The H2020 STRATOFLY Project and the H2020 MORE&LESS project have received funding from the European Union's Horizon 2020 research and innovation program under Grant Agreement No. 769246 and 101006856, respectively.

We want to acknowledge the contribution by Davis et al. (2016) that enabled us to use satellite measurements for validation of H_2O and O_3 mixing ratios of EMAC results.

The main part of post-processing, data analysis and plotting has been done using the module xarray (version 0.20.1 Hoyer and Hamman, 2017) and matplotlib.

For interpolating hybrid model level to pressure level we used the *interp_hybrid_to_pressure* function from geocat.comp (Visualization & Analysis Systems Technologies, 2021).

15. References

Blanvillain, E. and Gallic, G.: HIKARI: Paving the way towards high speed air transport, in: 20th AIAA international space planes and hypersonic systems and technologies conference, 20th AIAA international space planes and hypersonic systems and technologies conference, https://doi.org/10.2514/6.2015-3676, 2015.

Crutzen, P. J. and Arnold, F.: Nitric acid cloud formation in the cold Antarctic stratosphere: a major cause for the springtime "ozone hole," Nature, 324, 651–655, https://doi.org/10.1038/324651a0, 1986.

Dahlmann, K., Koch, A., Linke, F., Lührs, B., Grewe, V., Otten, T., Seider, D., Gollnick, V., and Schumann, U.: Climate-compatible air transport system—climate impact mitigation potential for actual and future aircraft, Aerospace, 3, 38, https://doi.org/10.3390/aerospace3040038, 2016.

Davis, S. M., Rosenlof, K. H., Hassler, B., Hurst, D. F., Read, W. G., Vömel, H., Selkirk, H., Fujiwara, M., and Damadeo, R.: The stratospheric water and ozone satellite homogenized (SWOOSH) database: A long-term database for climate studies, 30, 2016.

de F. Forster, P. M. and Shine, K. P.: Radiative forcing and temperature trends from stratospheric ozone changes, J. Geophys. Res., 102, 10841–10855, https://doi.org/10.1029/96JD03510, 1997.

Dietmüller, S., Jöckel, P., Tost, H., Kunze, M., Gellhorn, C., Brinkop, S., Frömming, C., Ponater, M., Steil, B., Lauer, A., and
Hendricks, J.: A new radiation infrastructure for the modular earth submodel system (MESSy, based on version 2.51),
940   Geosci. Model Dev., 9, 2209–2222, https://doi.org/10.5194/gmd-9-2209-2016, 2016.

Ehhalt, D. H., Rohrer, F., and Wahner, A.: TROPOSPHERIC CHEMISTRY AND COMPOSITION | Oxidizing Capacity, in:
Encyclopedia of Atmospheric Sciences (Second Edition), edited by: North, G. R., Pyle, J., and Zhang, F., Academic
Press, Oxford, 243–250, 2015.

Fahey, D. W., Baughcum, S. L., Fuglestvedt, J. S., Gupta, M., Lee, D. S., and Sausen, R.: White paper on climate change
945   aviation impacts on climate: State of the science, ICAO Environmental Report, 9, 2016.

Grewe, V. and Stenke, A.: AirClim: An efficient tool for climate evaluation of aircraft technology, Atmos. Chem. Phys., 8,
4621–4639, https://doi.org/10.5194/acp-8-4621-2008, 2008.

Grewe, V., Brunner, D., Dameris, M., Grenfell, J. L., Hein, R., Shindell, D., and Staehelin, J.: Origin and variability of upper
tropospheric nitrogen oxides and ozone at northern mid-latitudes, Atmospheric Environment, 35, 3421–3433,
950   https://doi.org/10.1016/S1352-2310(01)00134-0, 2001.

Grewe, V., Plohr, M., Cerino, G., Muzio, M. D., Deremaux, Y., Galerneau, M., Martin, P. de S., Chaika, T., Hasselrot, A.,
Tengzelius, U., and Korovkin, V. D.: Estimates of the climate impact of future small-scale supersonic transport
aircraft – results from the HISAC EU-project, Aeronaut. j., 114, 199–206,
https://doi.org/10.1017/S000192400000364X, 2010.

955 Grewe, V., Frömming, C., Matthes, S., Brinkop, S., Ponater, M., Dietmüller, S., Jöckel, P., Garny, H., Tsati, E., Dahlmann,
K., Søvde, O. A., Fuglestvedt, J., Berntsen, T. K., Shine, K. P., Irvine, E. A., Champougny, T., and Hullah, P.: Aircraft
routing with minimal climate impact: The REACT4C climate cost function modelling approach (V1.0), Geoscientific
Model Development, 7, 175–201, https://doi.org/10.5194/gmd-7-175-2014, 2014a.

Grewe, V., Champougny, T., Matthes, S., Frömming, C., Brinkop, S., Søvde, O. A., Irvine, E. A., and Halscheidt, L.: Reduction
960   of the air traffic's contribution to climate change: A REACT4C case study, Atmospheric Environment, 94, 616–625,
https://doi.org/10.1016/j.atmosenv.2014.05.059, 2014b.

Grewe, V., Bock, L., Burkhardt, U., Dahlmann, K., Gierens, K., Hüttenhofer, L., Unterstrasser, S., Rao, A. G., Bhat, A., Yin,
F., Reichel, T. G., Paschereit, O., and Levy, Y.: Assessing the climate impact of the AHEAD multi-fuel blended wing
body, metz, 26, 711–725, https://doi.org/10.1127/metz/2016/0758, 2017.

965 Grewe, V., Gangoli Rao, A., Grönstedt, T., Xisto, C., Linke, F., Melkert, J., Middel, J., Ohlenforst, B., Blakey, S., Christie, S.,
Matthes, S., and Dahlmann, K.: Evaluating the climate impact of aviation emission scenarios towards the paris
agreement including COVID-19 effects, Nat Commun, 12, 3841, https://doi.org/10.1038/s41467-021-24091-y, 2021.

Hansen, J., Sato, M., and Ruedy, R.: Radiative forcing and climate response, J. Geophys. Res., 102, 6831–6864,
https://doi.org/10.1029/96JD03436, 1997.

970   Hasselmann, K., Sausen, R., Maier-Reimer, E., and Voss, R.: On the cold start problem in transient simulations with coupled atmosphere-ocean models, Climate Dynamics, 9, 53–61, https://doi.org/10.1007/BF00210008, 1993.

Hegglin, M. I., Tegtmeier, S., Anderson, J., Froidevaux, L., Fuller, R., Funke, B., Jones, A., Lingenfelser, G., Lumpe, J., Pendlebury, D., Remsberg, E., Rozanov, A., Toohey, M., Urban, J., Clarmann, T. von, Walker, K. A., Wang, R., and Weigel, K.: SPARC data initiative: Comparison of water vapor climatologies from international satellite limb
975   sounders: SPARC DATA INITIATIVE WATER VAPOR COMPARISONS, J. Geophys. Res. Atmos., 118, 11, 824– 11, 846, https://doi.org/10.1002/jgrd.50752, 2013.

Hoyer, S. and Hamman, J.: Xarray: N-d labeled arrays and datasets in python, Journal of Open Research Software, 5, 10, https://doi.org/10.5334/jors.148, 2017.

Ingenito, A.: Impact of hydrogen fueled hypersonic airliners on the O3 layer depletion, International Journal of Hydrogen
980   Energy, 43, 22694–22704, https://doi.org/10.1016/j.ijhydene.2018.09.208, 2018.

Iwasaka, Yasunobu and Hayashi, Masahiko: Nitric Acid Transport From The Stratosphere to The Troposphere and Ice Sheet in Antarctica Through Polar Stratosphere, Polar Meteorol. Glaciol. [preprint], https://nipr.repo.nii.ac.jp/?action=pages_view_main&active_action=repository_view_main_item_detail&item_id=3 638&item_no=1&page_id=13&block_id=104, 1991.

985   Jöckel, P., Sander, R., Kerkweg, A., Tost, H., and Lelieveld, J.: Technical note: The modular earth submodel system (MESSy) – a new approach towards earth system modeling, Atmos. Chem. Phys., 12, 2005.

Jöckel, P., Tost, H., Pozzer, A., Sander, R., Steil, B., Stiller, G., Tanarhte, M., Taraborrelli, D., Aardenne, J. van, and Lelieveld, J.: The atmospheric chemistry general circulation model ECHAM5/MESSy1: Consistent simulation of ozone from the surface to the mesosphere, Atmos. Chem. Phys., 38, 2006.

990   Jöckel, P., Kerkweg, A., Pozzer, A., Sander, R., Tost, H., Riede, H., Baumgaertner, A., Gromov, S., and Kern, B.: Development cycle 2 of the modular earth submodel system (MESSy2), Geosci. Model Dev., 3, 717–752, https://doi.org/10.5194/gmd-3-717-2010, 2010.

Jöckel, P., Tost, H., Pozzer, A., Kunze, M., Kirner, O., Brenninkmeijer, C. A. M., Brinkop, S., Cai, D. S., Dyroff, C., Eckstein, J., Frank, F., Garny, H., Gottschaldt, K.-D., Graf, P., Grewe, V., Kerkweg, A., Kern, B., Matthes, S., Mertens, M.,
995   Meul, S., Neumaier, M., Nützel, M., Oberländer-Hayn, S., Ruhnke, R., Runde, T., Sander, R., Scharffe, D., and Zahn, A.: Earth system chemistry integrated modelling (ESCiMo) with the modular earth submodel system (MESSy) version 2.51, Geosci. Model Dev., 9, 1153–1200, https://doi.org/10.5194/gmd-9-1153-2016.

Kerkweg, A., Buchholz, J., Ganzeveld, L., Pozzer, A., Tost, H., and Jockel, P.: Technical note: An implementation of the dry removal processes DRY DEPosition and SEDImentation in the modular earth submodel system (MESSy), Atmos.
1000   Chem. Phys., 16, 2006.

Kinnison, D., Brasseur, G. P., Baughcum, S. L., Zhang, J., and Wuebbles, D.: The impact on the ozone layer of a potential fleet of civil hypersonic aircraft, Earth's Future, 8, https://doi.org/10.1029/2020EF001626, 2020.

Kirner, O., Ruhnke, R., Buchholz-Dietsch, J., Jöckel, P., Brühl, C., and Steil, B.: Simulation of polar stratospheric clouds in the chemistry-climate-model EMAC via the submodel PSC, Geoscientific Model Development, 4, 169–182, https://doi.org/10.5194/gmd-4-169-2011, 2011.

Lacis, A. A., Wuebbles, D. J., and Logan, J. A.: Radiative forcing of climate by changes in the vertical distribution of ozone, Journal of Geophysical Research: Atmospheres, 95, 9971–9981, https://doi.org/10.1029/JD095iD07p09971, 1990.

Lee, D. S., Fahey, D. W., Skowron, A., Allen, M. R., Burkhardt, U., Chen, Q., Doherty, S. J., Freeman, S., Forster, P. M., Fuglestvedt, J., Gettelman, A., De León, R. R., Lim, L. L., Lund, M. T., Millar, R. J., Owen, B., Penner, J. E., Pitari, G., Prather, M. J., Sausen, R., and Wilcox, L. J.: The contribution of global aviation to anthropogenic climate forcing for 2000 to 2018, Atmospheric Environment, 244, 117834, https://doi.org/10.1016/j.atmosenv.2020.117834, 2021.

Liebhardt, B., Gollnick, V., and Luetjens, K.: Estimation of the market potential for supersonic airliners via analysis of the global premium ticket market, in: 11th AIAA aviation technology, integration, and operations (ATIO) conference, 11th AIAA aviation technology, integration, and operations (ATIO) conference, https://doi.org/10.2514/6.2011-6806, 2011.

Matthes, S., Schumann, U., Grewe, V., Frömming, C., Dahlmann, K., Koch, A., and Mannstein, H.: Climate Optimized Air Transport, in: Atmospheric Physics: Background – Methods – Trends, edited by: Schumann, U., Springer, Berlin, Heidelberg, 727–746, 2012.

Matthes, S., Lührs, B., Dahlmann, K., Grewe, V., Linke, F., Yin, F., Klingaman, E., and Shine, K. P.: Climate-Optimized Trajectories and Robust Mitigation Potential: Flying ATM4E, Aerospace, 7, 156, https://doi.org/10.3390/aerospace7110156, 2020.

Matthes, S., Lee, D. S., De Leon, R. R., Lim, L., Owen, B., Skowron, A., Thor, R. N., and Terrenoire, E.: Review: The Effects of Supersonic Aviation on Ozone and Climate, Aerospace, 9, 41, https://doi.org/10.3390/aerospace9010041, 2022.

Myhre, G., Kvalevåg, M., Rädel, G., Cook, J., Shine, K. P., Clark, H., Karcher, F., Markowicz, K., Kardas, A., Wolkenberg, P., Balkanski, Y., Ponater, M., Forster, P., Rap, A., Leon, R., and Rodriguez: Intercomparison of radiative forcing calculations of stratospheric water vapour and contrails, metz, 18, 585–596, https://doi.org/10.1127/0941-2948/2009/0411, 2009.

Ocko, I. B. and Hamburg, S. P.: Climate consequences of hydrogen emissions, Atmospheric Chemistry and Physics, 22, 9349–9368, https://doi.org/10.5194/acp-22-9349-2022, 2022.

Organization (WMO), W. M., Administration, (NOAA). N. O. {and}. A., Programme, (UNEP). U. N. E., Administration, (NASA). N. A. {and}. S., Commission, E., and (WMO), W. M. O.: Scientific assessment of ozone depletion: 2014 - twenty questions and answers about the ozone layer: 2014 update (GORMP 56), WMO, Geneva, 84 p. pp., 2015.

Pachauri, R.K and Meyer, L.A. (Eds.): AR5 Synthesis Report: Climate Change, IPCC, Geneva, 2014.

Pachauri, R.K. and Reisinger, A. (Eds.): AR4 Climate Change: Synthesis Report, IPCC, Geneva, 2007.

1035 Penner, J.E., Lister, D.H., Griggs, D.J., Dokken, D.J., and McFarland, M. (Eds.): Aviation and the Global Atmosphere, IPCC, 1999.

Pletzer, J., Hauglustaine, D., Cohen, Y., Jöckel, P., and Grewe, V.: The climate impact of hydrogen-powered hypersonic transport, Atmospheric Chemistry and Physics, 22, 14323–14354, https://doi.org/10.5194/acp-22-14323-2022, 2022.

Pozzer, A., Jockel, P., Sander, R., Williams, J., Ganzeveld, L., and Lelieveld, J.: Technical note: The MESSy-submodel
1040 AIRSEA calculating the air-sea exchange of chemical species, Atmos. Chem. Phys., 10, 2006.

Pyle, J. A.: STRATOSPHERIC CHEMISTRY TOPICS | Overview, in: Encyclopedia of Atmospheric Sciences, Elsevier, 211–214, 2015.

Riese, M., Ploeger, F., Rap, A., Vogel, B., Konopka, P., Dameris, M., and Forster, P.: Impact of uncertainties in atmospheric mixing on simulated UTLS composition and related radiative effects, Journal of Geophysical Research: Atmospheres,
1045 117, https://doi.org/10.1029/2012JD017751, 2012.

Roeckner, E., Brokopf, R., Esch, M., Giorgetta, M., Hagemann, S., Kornblueh, L., Manzini, E., Schlese, U., and Schulzweida, U.: Sensitivity of simulated climate to horizontal and vertical resolution in the ECHAM5 atmosphere model, Journal of Climate, 19, 3771–3791, https://doi.org/10.1175/JCLI3824.1, 2006.

Sander, R., Kerkweg, A., Jockel, P., and Lelieveld, J.: Technical note: The new comprehensive atmospheric chemistry module
1050 MECCA, Atmos. Chem. Phys., 6, 2005.

Sander, R., Baumgaertner, A., Gromov, S., Harder, H., Jöckel, P., Kerkweg, A., Kubistin, D., Regelin, E., Riede, H., Sandu, A., Taraborrelli, D., Tost, H., and Xie, Z.-Q.: The atmospheric chemistry box model CAABA/MECCA-3.0, Geosci. Model Dev., 4, 373–380, https://doi.org/10.5194/gmd-4-373-2011, 2011.

Sander, R., Jöckel, P., Kirner, O., Kunert, A. T., Landgraf, J., and Pozzer, A.: The photolysis module JVAL-14, compatible
1055 with the MESSy standard, and the JVal PreProcessor (JVPP), Geosci. Model Dev., 7, 2653–2662, https://doi.org/10.5194/gmd-7-2653-2014, 2014.

Sridhar, B., Ng, H. K., and Chen, N. Y.: Aircraft Trajectory Optimization and Contrails Avoidance in the Presence of Winds, Journal of Guidance, Control, and Dynamics, 34, 1577–1584, https://doi.org/10.2514/1.53378, 2011.

Sun, Y. and Smith, H.: Review and prospect of supersonic business jet design, Progress in Aerospace Sciences, 90, 12–38,
1060 https://doi.org/10.1016/j.paerosci.2016.12.003, 2017.

Tabazadeh, A., Santee, M. L., Danilin, M. Y., Pumphrey, H. C., Newman, P. A., Hamill, P. J., and Mergenthaler, J. L.: Quantifying Denitrification and Its Effect on Ozone Recovery, Science, 288, 1407–1411, https://doi.org/10.1126/science.288.5470.1407, 2000.

Tegtmeier, S., Hegglin, M. I., Anderson, J., Bourassa, A., Brohede, S., Degenstein, D., Froidevaux, L., Fuller, R., Funke, B.,
1065 Gille, J., Jones, A., Kasai, Y., Krüger, K., Kyrölä, E., Lingenfelser, G., Lumpe, J., Nardi, B., Neu, J., Pendlebury, D., Remsberg, E., Rozanov, A., Smith, L., Toohey, M., Urban, J., Clarmann, T. von, Walker, K. A., and Wang, R. H. J.: SPARC data initiative: A comparison of ozone climatologies from international satellite limb sounders: OZONE

CLIMATOLOGIES FROM LIMB SOUNDERS, J. Geophys. Res. Atmos., 118, 12, 229–12, 247, https://doi.org/10.1002/2013JD019877, 2013.

1070 Tost, H., Jockel, P., Kerkweg, A., Sander, R., and Lelieveld, J.: Technical note: A new comprehensive SCAVenging submodel for global atmospheric chemistry modelling, Atmos. Chem. Phys., 10, 2006.

Tost, H., Jockel, P., and Lelieveld, J.: Lightning and convection parameterisations – uncertainties in global modelling, Atmos. Chem. Phys., 16, 2007.

van Manen, J. and Grewe, V.: Algorithmic climate change functions for the use in eco-efficient flight planning, Transportation
1075 Research Part D: Transport and Environment, 67, 388–405, https://doi.org/10.1016/j.trd.2018.12.016, 2019.

Visualization & Analysis Systems Technologies: Geoscience Community Analysis Toolkit, UCAR/NCAR - Computational and Informational System Lab, Bouler, CO, 2021.

Wilcox, L. J., Shine, K. P., and Hoskins, B. J.: Radiative forcing due to aviation water vapour emissions, Atmospheric Environment, 63, 1–13, https://doi.org/10.1016/j.atmosenv.2012.08.072, 2012.

1080 Winterstein, F. and Jöckel, P.: Methane chemistry in a nutshell – the new submodels CH4 (v1.0) and TRSYNC (v1.0) in MESSy (v2.54.0), Geoscientific Model Development, 14, 661–674, https://doi.org/10.5194/gmd-14-661-2021, 2021.

World Meteorological Organization, United States, National Oceanic and Atmospheric Administration, United States, National Aeronautics and Space Administration, United Nations Environment Programme, and European Commission: Scientific assessment of ozone depletion: 2018., 2019.

1085 Zhang, J., Wuebbles, D., Kinnison, D., and Baughcum, S. L.: Potential impacts of supersonic aircraft emissions on ozone and resulting forcing on climate: An update on historical analysis, Geophys Res Atmos, 126, https://doi.org/10.1029/2020JD034130, 2021a.

Zhang, J., Wuebbles, D., Kinnison, D., and Baughcum, S. L.: Stratospheric Ozone and Climate Forcing Sensitivity to Cruise Altitudes for Fleets of Potential Supersonic Transport Aircraft, Journal of Geophysical Research: Atmospheres, 126,
1090 https://doi.org/10.1029/2021JD034971, 2021b.